Supplement of Atmos. Chem. Phys., 26, 11281–11307, 2026
https://doi.org/10.5194/acp-26-11281-2026-supplement

Atmospheric Chemistry and Physics

Supplement of

Process evaluation suggests models misrepresent the precipitation-driven replenishment of cloud condensation nuclei

Sara M. Blichner et al.

Correspondence to: Sara M. Blichner (sara.blichner@aces.su.se)

Contents

S1 Model descriptions

S1.0.1 ECHAM-SALSA

General description: The global aerosol-climate model ECHAM-SALSA (ECHAM6.3-HAM2.3; Schultz et al., 2018) is widely used to simulate the complex interactions between aerosols, clouds, and the broader climate system. ECHAM-SALSA consists of the general circulation model ECHAM6.3, which captures large-scale atmospheric dynamics by solving equations for divergence, temperature, surface pressure, and vorticity. ECHAM employs a spectral method for calculating the atmospheric circulation and we use the T63 spectral truncation for the horizontal grid, with 47 flexible vertical levels.

ECHAM is coupled with HAM (Hamburg Aerosol Model), which simulates the atmospheric aerosol life cycle, including emissions, formation, growth, and removal (Kokkola et al., 2018; Tegen et al., 2019). The chemical compounds included in

HAM are sulfate (SU), organic aerosol (OA), sea salt (SS), black carbon (BC), and mineral dust (DU). HAM includes detailed representations of secondary organic aerosol (SOA) formation, aerosol–radiation interactions, and aerosol–cloud interactions. ECHAM-HAM is further coupled with the Sectional Aerosol module for Large Scale Applications (SALSA; Kokkola et al., 2018). SALSA provides a size-resolved treatment of aerosol microphysics using a sectional approach. The aerosol size spectrum is divided into 10 size bins ranging from $3\,\mathrm{nm}$ to $10\,\mathrm{\mu m}$, with parallel externally mixed size classes for particles larger than $50\,\mathrm{nm}$ (Kokkola et al., 2018). SALSA simulates key processes such as nucleation, coagulation, condensation/evaporation, and hydration. Cloud droplet activation is represented using the parameterization by Abdul-Razzak and Ghan (2002), which calculates the fraction of particles activated within each size bin. The module tracks several chemical species, including sulfate, organic carbon, black carbon, sea salt, and mineral dust.

ECHAM-SALSA includes the Volatility Basis Set (VBS) framework to represent SOA formation based on the volatility distribution of organic compounds. By default, ECHAM-SALSA uses a three volatility bin VBS setup for monoterpene oxidation products with C_{sat} values of 0, 1, and $10\,\mathrm{\mu m^{-3}}$ (Mielonen et al., 2018; Irfan et al., 2024).

In the simulations in this study, nudging was applied toward the ERA-Interim reanalysis data from the European Centre for Medium-Range Weather Forecasts (Berrisford et al., 2011). The relaxation times applied for nudging surface pressure, vorticity, and divergence were 24, 6, and 48 hours, respectively.

Wet deposition:

Nucleation scavenging in stratiform clouds: For stratiform clouds ECHAM-SALSA uses size dependent schemes for in-cloud nucleation scavenging detailed in Holopainen et al. (2020). For liquid phase, the in-cloud nucleation scavenging coefficients are calculated using the fraction of activated particles in each size class using the parameterization (Abdul-Razzak and Ghan, 2002). For ice phase, size-dependent scavenging coefficients are calculated based on the surface area of each size class.

In-cloud impaction scavenging in stratiform clouds: The coefficients are based on coagulation rates using wet aerosol particle size and cloud droplet radii and are thus size dependent. Additionally, separate coefficients are calculated for ice crystals, assuming these are monodisperse(see Croft et al., 2010; Holopainen et al., 2020).

Convective cloud scavenging: For convective clouds ECHAM-SALSA uses fixed scavenging coefficients (Bergman et al., 2012). There is no phase dependency on these parameters.

Below cloud scavenging: For below-cloud scavenging in both convective and stratiform clouds, the method of Croft et al. (2009) is used, with each size bin approximated as a log-normal mode. The size-dependent collection efficiency is based on the aerosol and collector drop (raindrops follow the distribution of Marshall and Palmer (1948)) following Croft et al. (2009) and is calculated separately for stratiform and convective clouds, for rain and snow (Croft et al., 2009; Zhang et al., 2012).

Resuspension of aerosols when precipitation evaporates: Resuspension of aerosols when precipitation evaporates is treated so that aerosols from evaporated clouds are released back from the clouds only if the evaporation occurs in the same grid box as precipitation formation. There is no vertical redistribution of aerosol due to precipitation.

Phase dependency: In ice clouds, nucleation scavenging in stratiform clouds involves the formation and growth of ice particles, which can grow to precipitation sizes and be removed. The model accounts for ice nucleation rates and defines the scavenging coefficient values based on the surface area of particles in each size class (see Holopainen et al., 2020). Also for below-cloud scavenging, the model considers the collection efficiency of raindrops and snowflakes differently.

S1.0.2 EC-Earth

General description:

In this study, we employ the atmosphere-only AerChem configuration of the Earth system model EC-Earth3.4, which couples a general circulation model (GCM) with an atmospheric chemistry transport model (van Noije et al., 2021, 2014). The GCM component is based on cycle 36r4 of the Integrated Forecasting System (IFS), utilizing a spectral truncation of T255 (approximately 0.7° horizontal resolution) on an N128 reduced Gaussian grid, with 91 vertical levels represented on a hybrid sigma-pressure coordinate system (Döscher et al., 2022). Atmospheric chemistry and aerosol processes are simulated using version 1.2 of the Tracer Model 5 with massively parallel (TM5-MP), which includes the M7 aerosol microphysics module (Vignati et al., 2004; Krol et al., 2005; Williams et al., 2017). TM5-MP operates on a $2^\circ \times 3^\circ$ (latitude × longitude) horizontal grid and 34 hybrid sigma-pressure levels, which are derived from the same vertical structure used in IFS.

In the simulations in this study, nudging was applied to the IFS model using a relaxation time of 6 hours to ERA-Interim (Berrisford et al., 2011) meteorological fields for divergence, vorticity (horizontal winds), and surface pressure.

Wet deposition:

Precipitation fields for calculating wet deposition in TM5 are received from the IFS model with a coupling time of 6 hours.

In-cloud scavenging: Wet removal of aerosols in EC-Earth is parameterized using prescribed mode-dependent scavenging fractions following Croft et al. (2010) with coefficients from Stier et al. (2005) for convective clouds and Bourgeois and Bey (2011) for stratiform in-cloud scavenging (see Table 2 in van Noije et al. (2021)). There is also no distinction between in-cloud activation and impaction scavenging, but rather these are combined in one scavenging fraction. The stratiform in-cloud scavenging is phase dependent, with higher removal for liquid clouds than ice (see Table 2 van Noije et al., 2021).

Below cloud scavenging: Below cloud scavenging by stratiform precipitation applies scavenging coefficient for each mode separately, and for number and mass separately (see Table 3 in van Noije et al. (2021)). These are based on results from Croft et al. (2009) and calculated for a Marshall-Palmer rain droplet size distribution and precipitation rate of $1\,\mathrm{mmh}^{-1}$. This in effect shifts the size distribution, with nucleation and Aitken modes to larger sizes and accumulation and coarse to smaller (van Noije et al., 2021). For convective clouds, below cloud scavenging is included in the fractions described above.

Resuspension of aerosols when precipitation evaporates: Not treated in this version of the model, but investigated in de Bruine et al. (2018).

Phase dependency: There is a phase dependency for stratiform in-cloud scavenging (see again Table 2 in van Noije et al., 2021), with different coefficients for each mode. For below-cloud scavenging there is no phase dependency.

S1.0.3 NorESM

General description: The Norwegian Earth System model version 2 (NorESM2 Bentsen et al., 2013; Kirkevåg et al., 2013; Iversen et al., 2013) is based on the Community Earth System Model (CESM Danabasoglu et al., 2020), but features a different ocean model – the Bergen Layered Ocean Model (BLOM) – along with significant modifications to the atmospheric component, including a distinct chemistry and aerosol model (Seland et al., 2020). In this study sea surface temperatures and sea ice data based on the Hadley Centre Sea Ice and Sea Surface Temperature data set (HADISST, Rayner et al., 2003) as described in Hurrell et al. (2008) were read from file, so the ocean component is not in use. The atmospheric component used in NorESM, CAM6-Nor, is heavily based on the Community Atmospheric model version 6 (CAM6, see e.g Bogenschutz et al., 2018) but the aerosol scheme is replaced by OsloAero6 (described below, see also Kirkevåg et al., 2018) and it also includes improvements to the local dry and moist energy conservation, angular momentum conservation and in the computation of air-sea fluxes and deep convection. CAM6-Nor uses the same cloud macrophyiscs scheme as CAM6, namely the Cloud Layers Unified by Binomials model (CLUBB; Bogenschutz et al., 2018), as well as the same microphysics in shallow convection and stratiform clouds, which is the two-moment bulk scheme from MG2, Gettelman and Morrison (2015). Finally, the representation of microphysics in deep convective clouds is based on Zhang and McFarlane (1995). Cloud droplet activation is calculated using the Abdul-Razzak scheme (Abdul-Razzak and Ghan, 2000). More details on the treatment of clouds in CAM6 and CAM6-Nor can be found in Bogenschutz et al. (2018).

OsloAero6 is an aerosol and chemistry model that employs a production-tagging approach to track the origin and transformation of aerosols throughout their atmospheric lifetime. A key distinguishing feature of this scheme is its division of aerosol tracers into two categories: "background" tracers and "process" tracers. Background tracers define the initial particle number and size distribution, which follows log-normal modes. In contrast, process tracers modify this distribution and adjust chemical composition based on precomputed look-up tables from the offline AeroTab scheme (Kirkevåg et al., 2018), allowing for deviations from a strict log-normal shape.

In the simulations in this study, nudging was applied using ERA-Interim (Berrisford et al., 2011) data for horizontal winds and surface pressure with a 6-hour relaxation time.

Wet deposition:

Nucleation scavenging in stratiform clouds NorESM keeps track of cloud-borne aerosols (prognostic variable) for stratiform clouds and uses this to calculate the nucleation scavenging. The nucleation scavenging is thus composition and size dependent through the activation scheme following Abdul-Razzak and Ghan (2000). The cloud-borne aerosols are then scavenged based on the precipitation rate.

In-cloud impaction scavenging in stratiform clouds: Additionally, the cloud-borne particles include particles coagulating with cloud droplets, which is calculated assuming a fixed cloud droplet size of $10\,\mu m$. The total in-cloud wet deposition then depends on a first-order loss rate calculated from cloud fraction, cloud water, and precipitation production profiles.

Convective clouds scavenging: For convective clouds, both nucleation scavenging and activation scavenging are parameterized by scavenging coefficients. Cloud-borne aerosols are not scavenged by convective precipitation, only interstitial aerosols are. Activation scavenging is controlled by an activation fraction coefficient (set to be 0.8) which controls the fraction of aerosols assumed to activate and a scavenging fraction (sol_factic, set to be 0.4) which is considered a tuning factor. These factors are independent of aerosol size and composition.

Below cloud scavenging: This is parameterized following Dana and Hales (1976); Balkanski et al. (1993) Barth et al. (as described in 2000). It is calculated based on a solubility factor (a tuning factor set to 0.1), multiplied by a scavenging coefficent which varies with mode (see Tab. S1) and the precipitation rate. Cloud-borne aerosols are not subject to below-cloud scavenging.

Resuspension of aerosols when precipitation evaporates: CAM-Oslo treats this, and in the case of evaporating precipitation the aerosol is resuspended proportional to the evaporation rate of precipitation from the layer above and the loss of aerosols from the layer above (if some x percent of the rain evaporates, then x percent of the scavenged aerosol is re-released in the grid box below (Barth et al., 2000).

Phase dependency: Wet deposition is not influenced by precipitation phase, neither for -below, nor for in-cloud scavenging.

Mode/Process	**Below-cloud Scavenging Coefficient**
Mode 00 (BC emitted externally mixed as fractal accumulation mode)	0.01
Mode 01 (NPF particles formed by SO_4 and SOA, usually Aitken mode)	0.02
Mode 02 (BC coated, Aitken mode)	0.02
Mode 04 (BC and OM (Organic matter) emitted internally, Aitken mode)	0.02
Mode 05 (SO_4 primary emitted, Accumulation mode)	0.01
Mode 06 (Dust, accumulation mode)	0.02
Mode 07 (Dust, Coarse mode)	0.2
Mode 08 (Sea salt, Aitken mode)	0.02
Mode 09 (Sea salt, accumulation mode)	0.02
Mode 10 (Sea salt, coarse mode)	0.5
Mode 12 (BC emitted externally mixed, nucleation mode)	0.08
Mode 14 (OM and BC emitted internally mixed, Aitken mode)	0.02
Process tracer SO_4_A1 condensate on extisting particles from gas phase	0.02
Process tracer SO_4_A2 formed from aquous phase chemistry	0.01
Process tracer SO_4_AC formed from coagulation with outer particles	0.02
Process tracer OM_AC OM and SOA formed from coagulation with outer particles	0.02
Process tracer BC_AC formed from coagulation with outer particles	0.02
Process tracer SOA_A1 condensate on existing particles from gas phase	0.02

Table S1. Below-cloud Scavenging Coefficients NorESM

S2 Scavenging of nucleation and small Aitken mode particles: separating night and day

To separate the impact of NPF inhibition from impact of scavenging of the smallest particles, one approach is to investigate the impact of precipitation during night time, as NPF is very rare during night, especially with subsequent growth. This is shown in

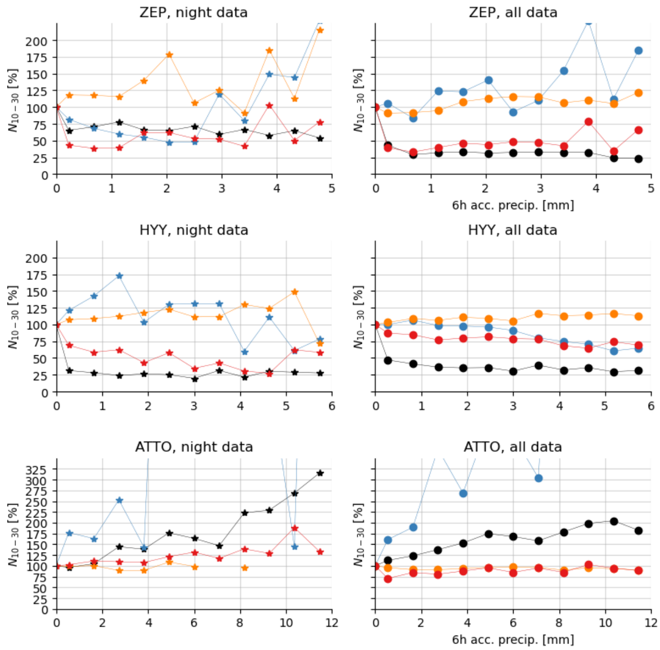

Figure S1. N_{10-30} binned by recent (6 h) accumulated precipitation. The dataset is divided into all data (right column) and only night time values (left column, defined as between 21:00 and 06:00 plus accumulated radiation over the last 6 hours below 30 $\mathrm{W m^{-2}}$).

Fig. S1 which has N_{10-30} binned by recent (6 h) accumulated precipitation and separated into night time (defined as between 21:00 and 06:00) and all data. The night-time conditions additionally have a requirement that 6 h accumulated radiation is below $30\mathrm{Wm^{-2}}$.

At Zeppelin, the reduction in N_{10-30} with increased 6 h accumulated precipitation is weaker for night-time than for for all values. This may be expected because during the day, we expect both the NPF inhibition and the direct wet deposition loss processes to be at play, while during night, NPF inhibition is expected to be minimal, because there is little to no NPF. ECHAM-SALSA seems to do better during night, where we see a reduction in N_{10-30}, rather than the slight increase observed when sunlit hours were included. NorESM on the other hand, remains unchanged, indicating – in consistence with Fig. 4 – that there is little influence of NPF here. EC-Earth has increasing N_{10-30} with increasing recent precipitation independent of whether it's night or all data – again, consistent with the unrealistic positive correlations for recent precipitation in Fig. 4.

For Hyytiälä, the reduction in N_{10-30} is similar between night and all data in the observations, though a little stronger during night. This is somewhat surprising given that, as mentioned above, during the day, both NPF inhibition and direct wet deposition are expected to reduce N_{10-30} with increased precipitation. Therefore, we would have expected the signal to be stronger for all data than for night only. NorESM is clearly closer to the observations for the night-time values, indicating that NPF plays a role in the weak negative correlation in Fig. 3 between recent precipitation and N_{10-30} particles in NorESM. However, for both ECHAM-SALSA and EC-Earth the pattern is opposite, with night time values showing a more positive

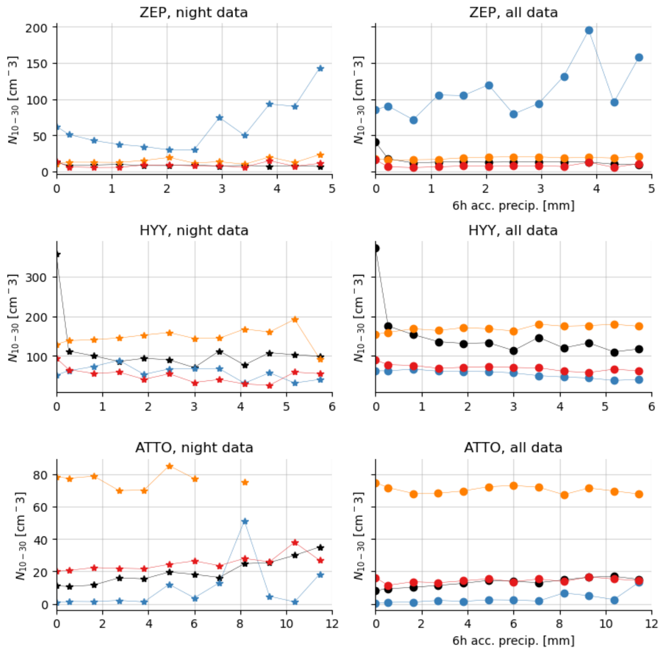

Figure S2. N_{10-30} binned by recent (6 h) accumulated precipitation. The dataset is divided into all data (right column) and only night time values (left column, defined as between 21:00 and 06:00 plus accumulated radiation over the last 6 hours below $30\,\mathrm{W m^{-2}}$).

relationship with increased 6 h accumulated precipitation. These are thus likely not NPF related, but rather related to the overall positive correlations for mass and number discussed below in Sect. 3.5.

Lastly, for ATTO, we do not necessarily expect a change between night and day if the appearance of the smallest particles is not related to photochemically induced NPF, but rather to downdrafts. However, convection typically happens during the late afternoon and evening (Machado et al., 2024), and one might then expect less of it during night. This is in fact what we see, with decreases for the first 4 bins of accumulated precip during night, and then an increase for the highest precipitation bins (potentially indicating convective precipitation). For the full dataset, however, we see an increase in N_{10-30} with increasing precipitation. ECHAM-SALSA and NorESM both have positive relationships for the night-time values. NorESM has more of a zero influence for the full dataset, while ECHAM-SALSA has a very high relative increase with increasing accumulated precipitation (likely related to very low particle number concentration). EC-Earth has very weak impact of precipitation on N_{10-30} at ATTO independent of the time of day.

It is hard to draw conclusions about model skill from these findings, though at least for EC-Earth, it seems like direct scavenging is not strong enough at any of the stations. From the ATTO results, they seem to indicate that the positive relationships between N_{10-30} and recent rainfall in NorESM and EC-Earth are not in fact highly related to local NPF, because if they were there would be a clearer difference between night and all values.

S3 Basic evaluation

S3.1 Precipitation

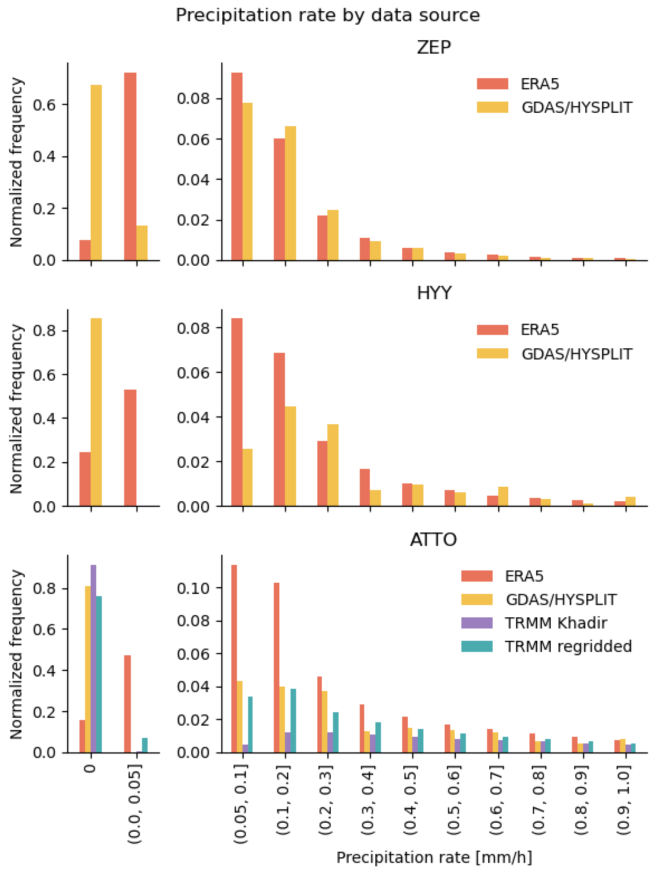

Figure S3. Precipitation rate [mm] at each station for different reanalysis and satellite products .

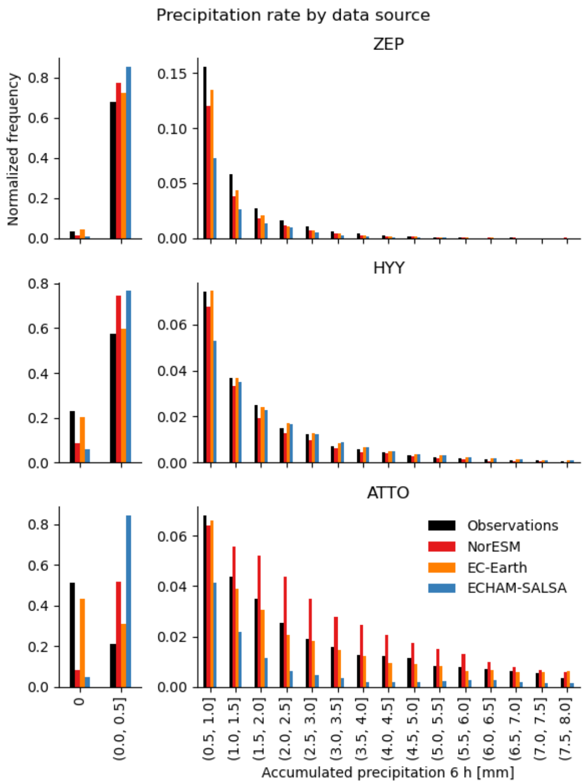

(a) Models versus observations

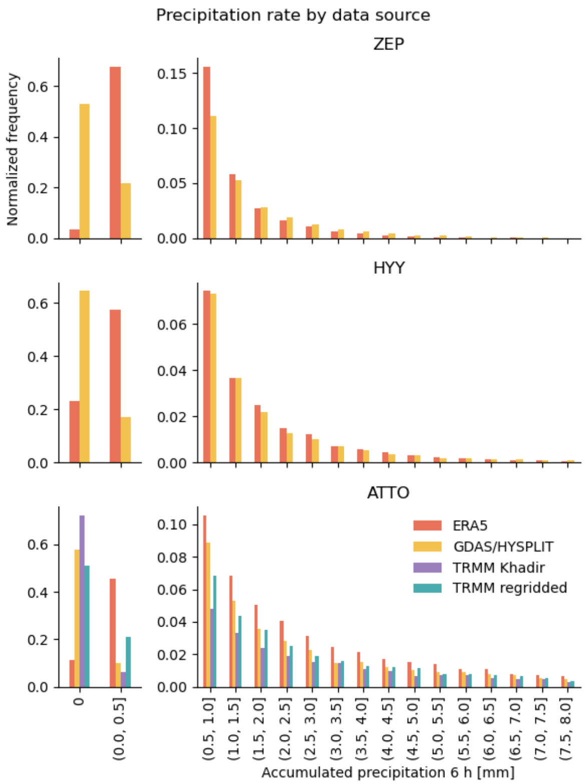

(b) Data sources for observations

Figure S4. Frequency of 6 hours accumulated precipitation at each station [mm].

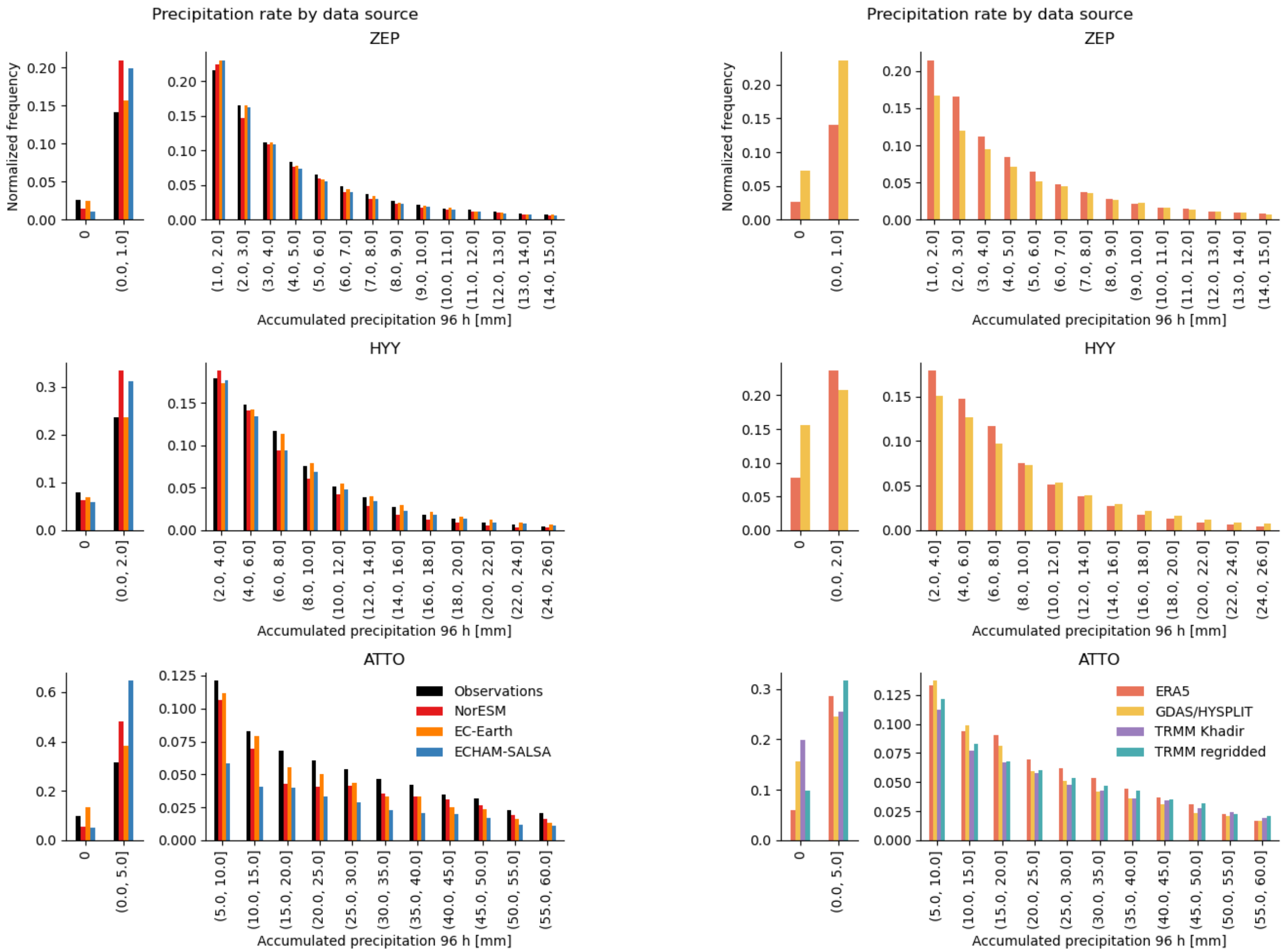

(a) Models versus observations

(b) Data sources for observations

Figure S5. Frequency of 96 hours accumulated precipitation at each station [mm].

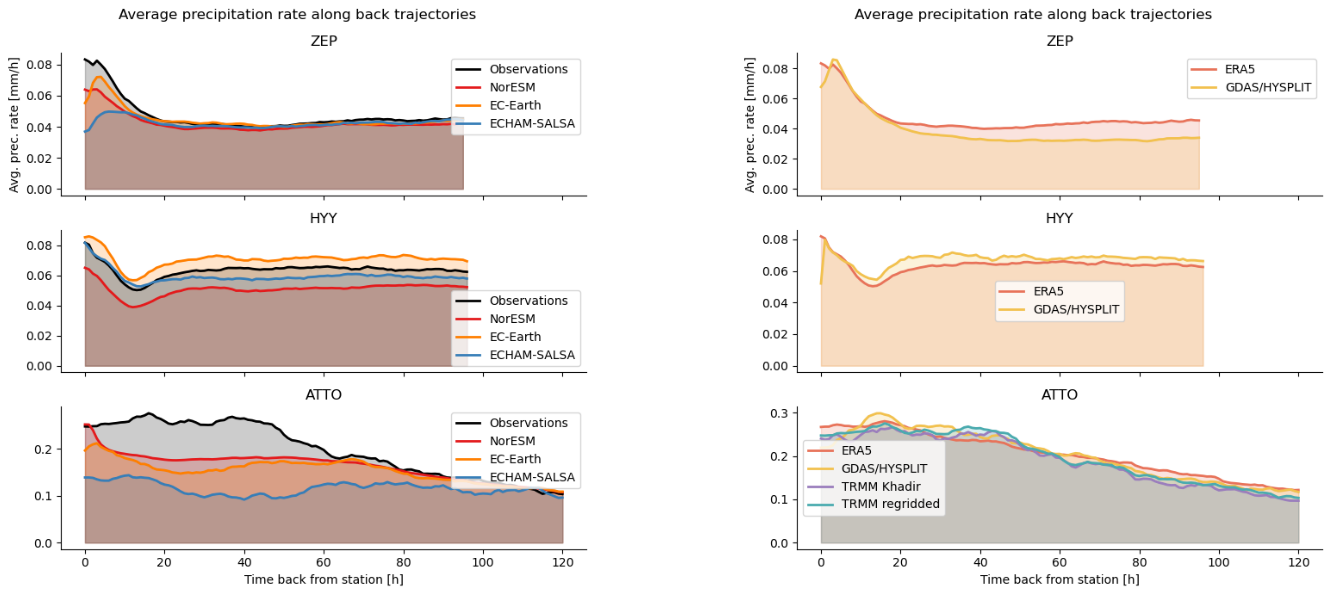

(a) Models versus observations

(b) Data sources for observations

Figure S6. Average precipitation rate along back trajectories [mm/h].

S3.2 Diurnal variation

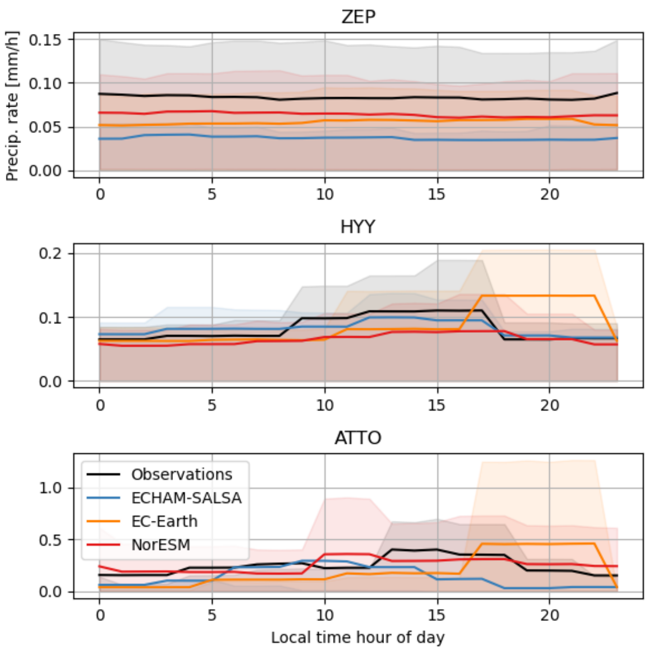

Figure S7. Mean diurnal variation in precipitation rate taken at the each station. The shaded area indicates the 16th-84th percentile.

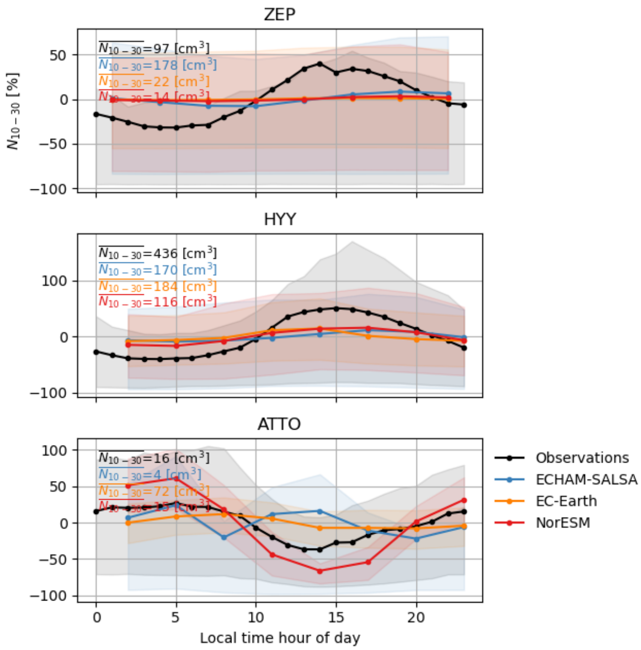

Figure S8. Mean diurnal variation in N_{10-30} at the each station in percentage deviation from the mean value of the total dataset (not each day). The shaded area indicates the 16th-84th percentile and the numbers indicate the mean at each station for each data source.

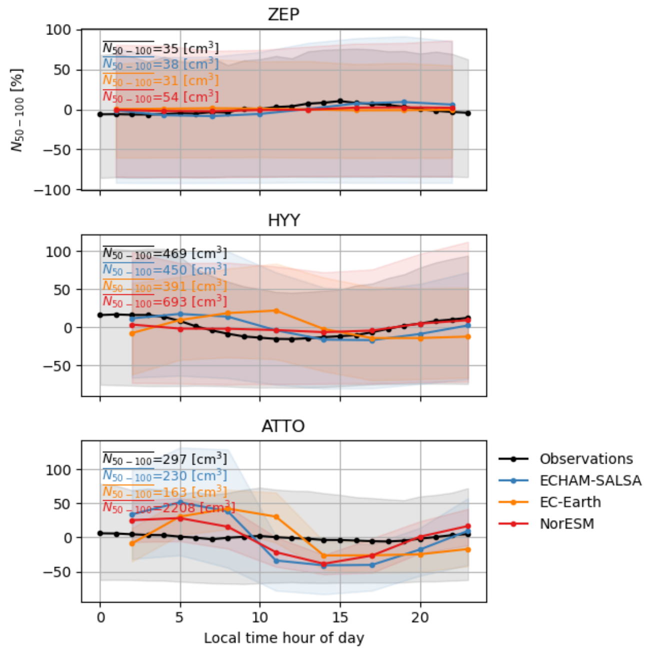

Figure S9. Mean diurnal variation in N_{50-100} at each station in percentage deviation from the mean value of the total dataset (not each day). The shaded area indicates the 16th-84th percentile and the numbers indicate the mean at each station for each data source.

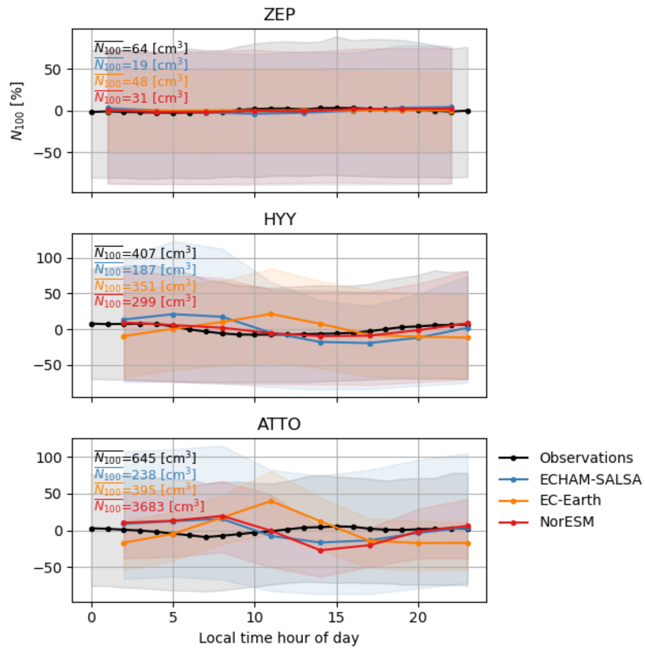

Figure S10. Mean diurnal variation in N_{100} at each station in percentage deviation from the mean value of the total dataset (not each day). The shaded area indicates the 16th-84th percentile and the numbers indicate the mean at each station for each data source.

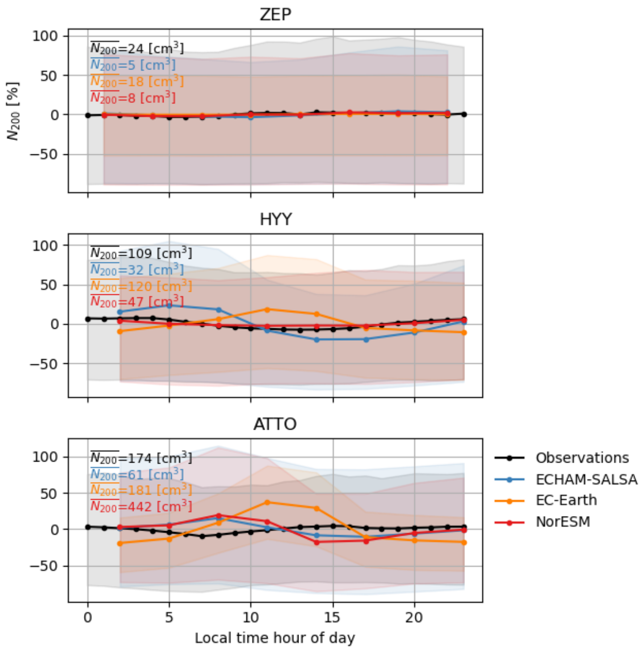

Figure S11. Mean diurnal variation in N_{200} at each station in percentage deviation from the mean value of the total dataset (not each day). The shaded area indicates the 16th-84th percentile and the numbers indicate the mean at each station for each data source.

S4 Correlations with GDAS versus ERA

S4.1 Hyytiälä

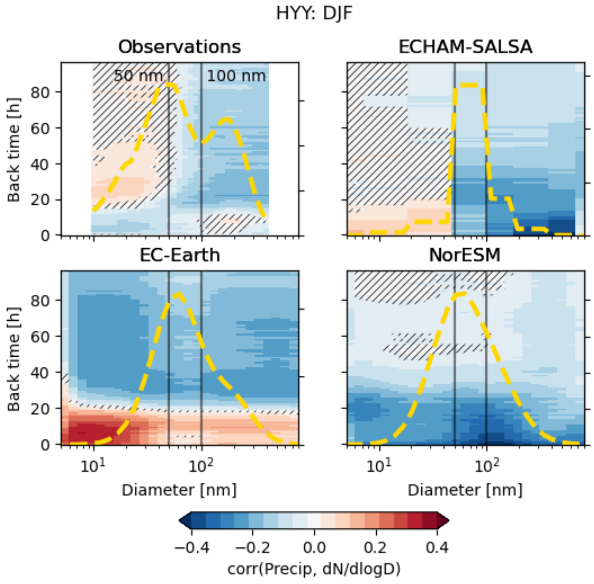

(a) HYSPLIT, GDAS

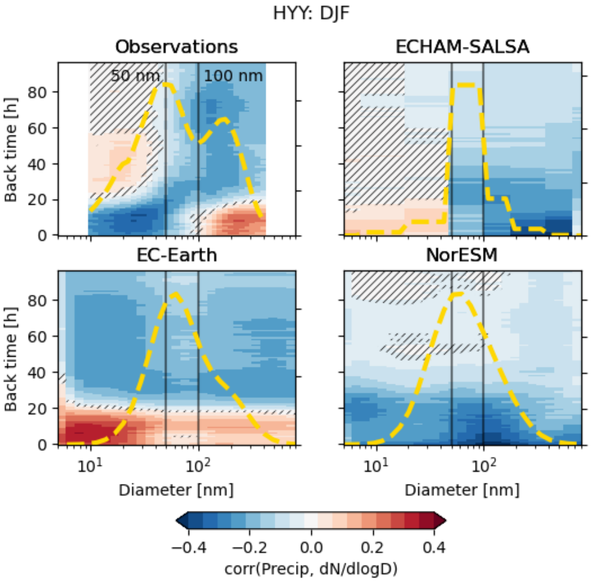

(b) ERA5

Figure S12. Comparison of GDAS and ERA5 correlations between precipitation and dNdlogD.

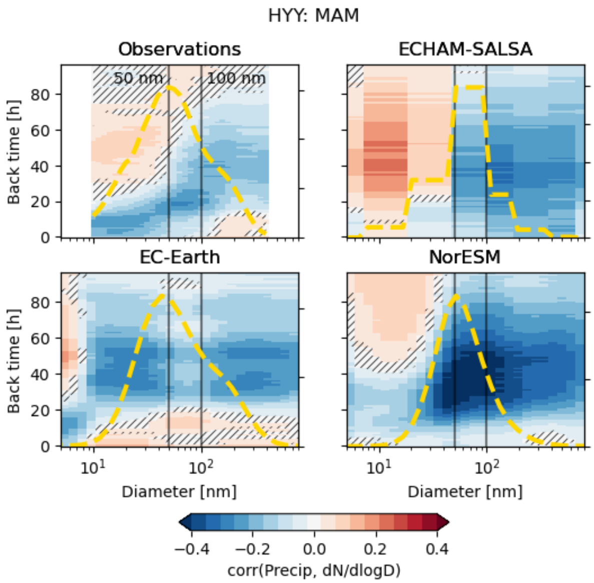

(a) Hysplit, GDAS

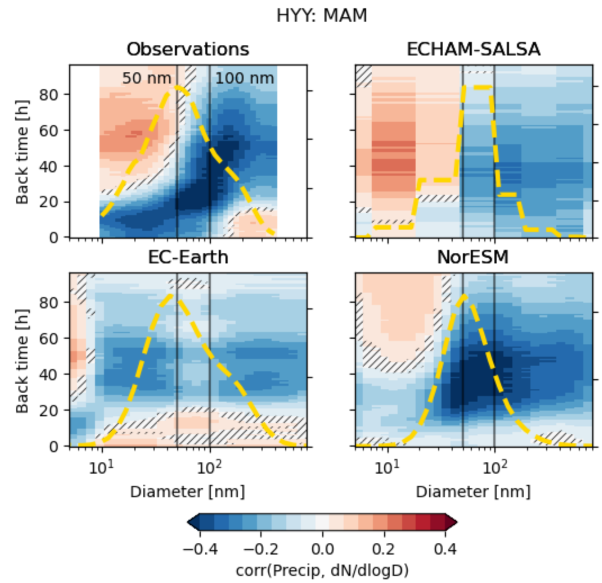

(b) ERA5

Figure S13. Comparison of GDAS and ERA5 correlations between precipitation and dNdlogD.

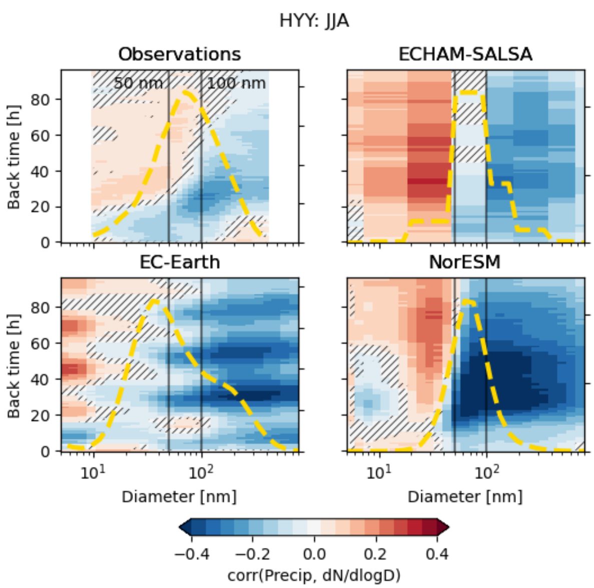

(a) HYSPLIT, GDAS

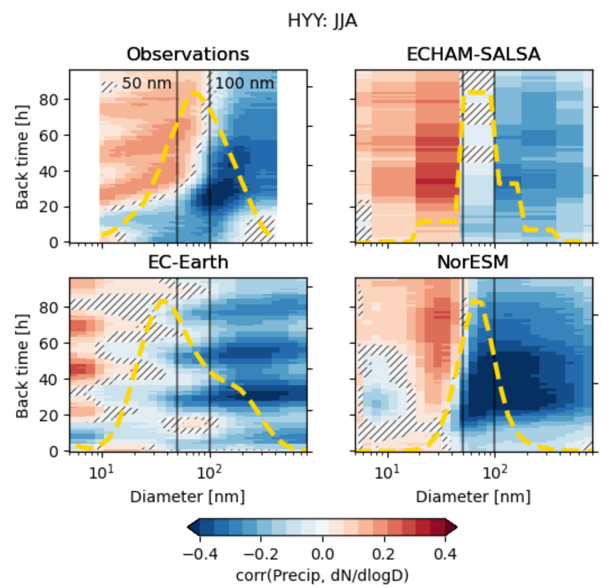

(b) ERA5

Figure S14. Comparison of GDAS and ERA5 correlations between precipitation and dNdlogD.

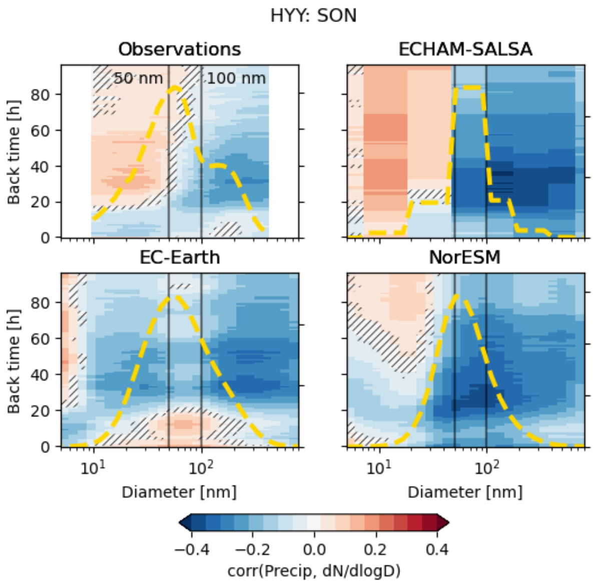

(a) HYSPLIT, GDAS

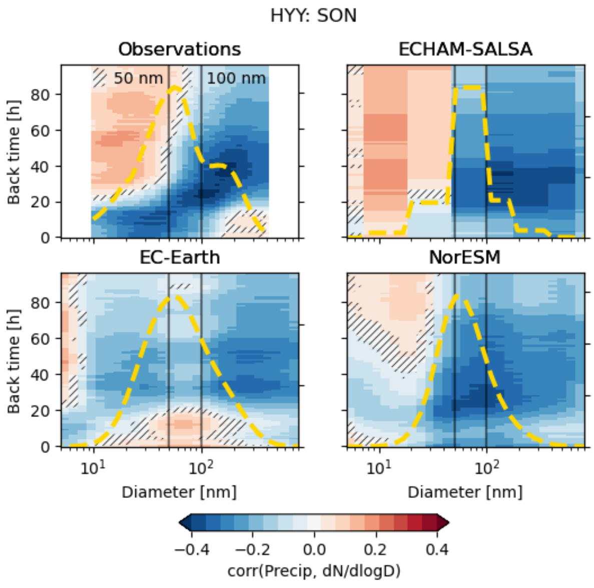

(b) ERA5

Figure S15. Comparison of GDAS and ERA5 correlations between precipitation and dNdlogD.

S4.2 Zeppelin

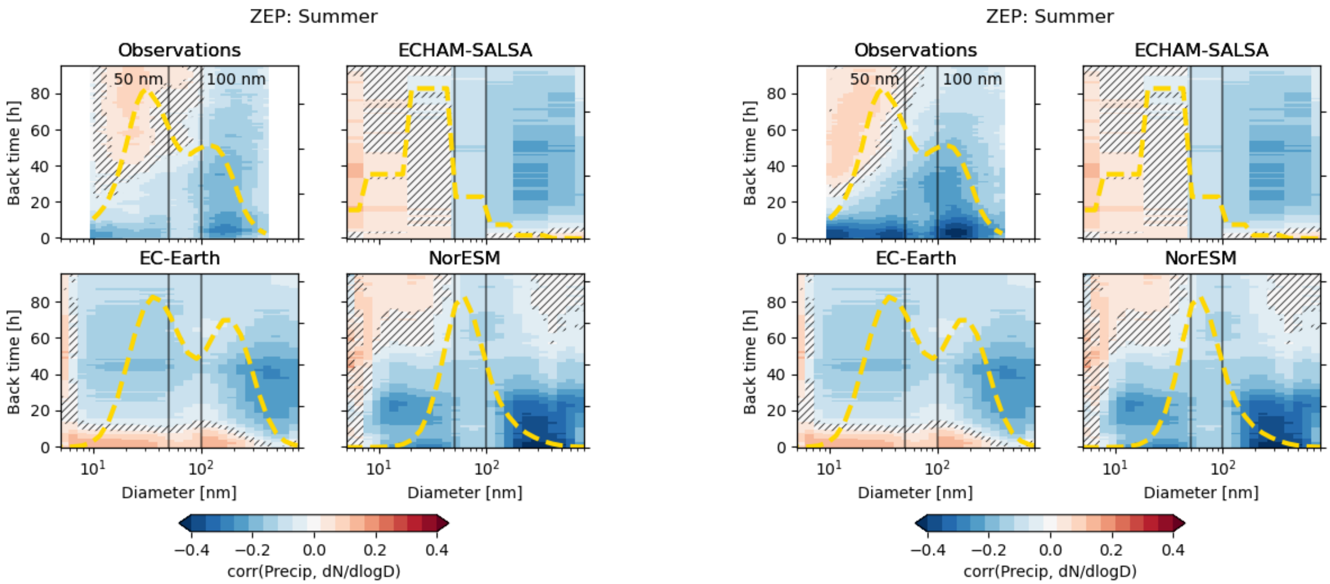

(a) HYSPLIT, GDAS

(b) ERA5

Figure S16. Comparison of GDAS and ERA5 correlations between precipitation and dNdlogD.

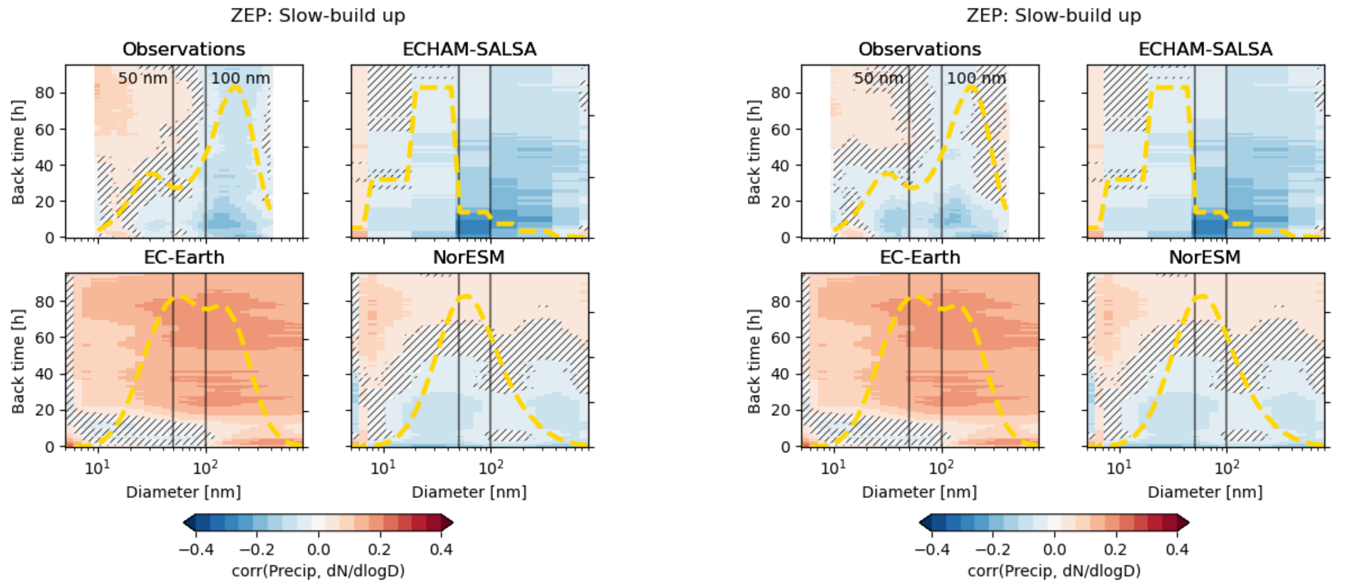

(a) HYSPLIT, GDAS (b) ERA5

Figure S17. Comparison of GDAS and ERA5 correlations between precipitation and dNdlogD.

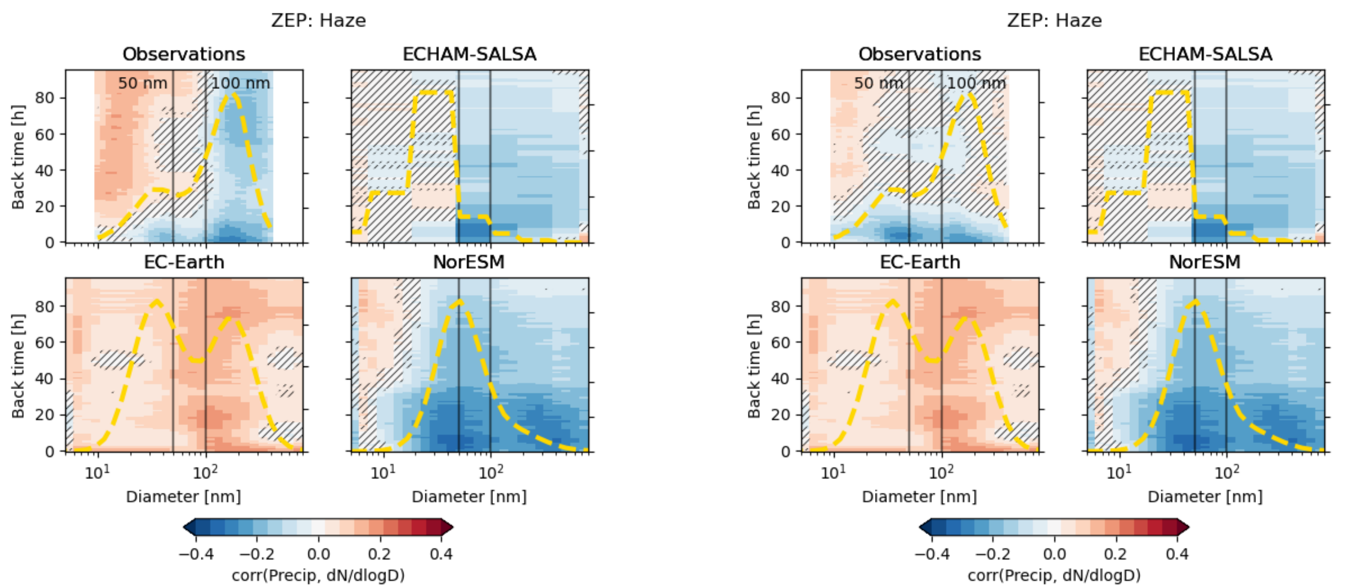

(a) HYSPLIT, GDAS (b) ERA5

Figure S18. Comparison of GDAS and ERA5 correlations between precipitation and dNdlogD.

S5 Correlations with and without drizzle included in models

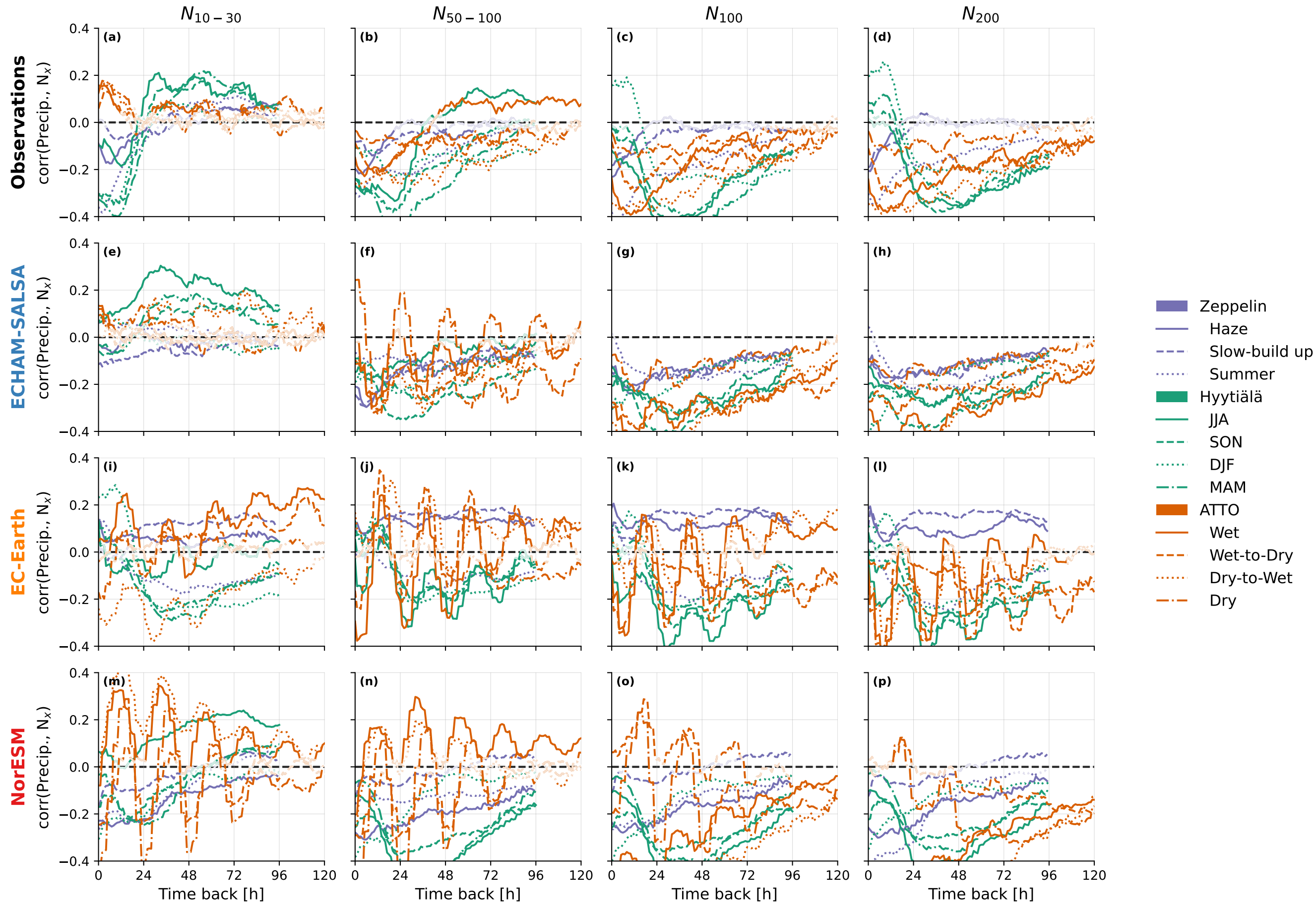

Figure S19. Spearman correlations between precipitation rate and N_{10-30} (first column), N_{50-100} (second column), N_{100} (third column) and N_{200} (last column,) for observations (top row, a and b) and models (c-h). Each line represents a season at a station, with color indicating the station and linestyle indicating the season. Faint lines indicate where the correlation is not significant (p>0.05).

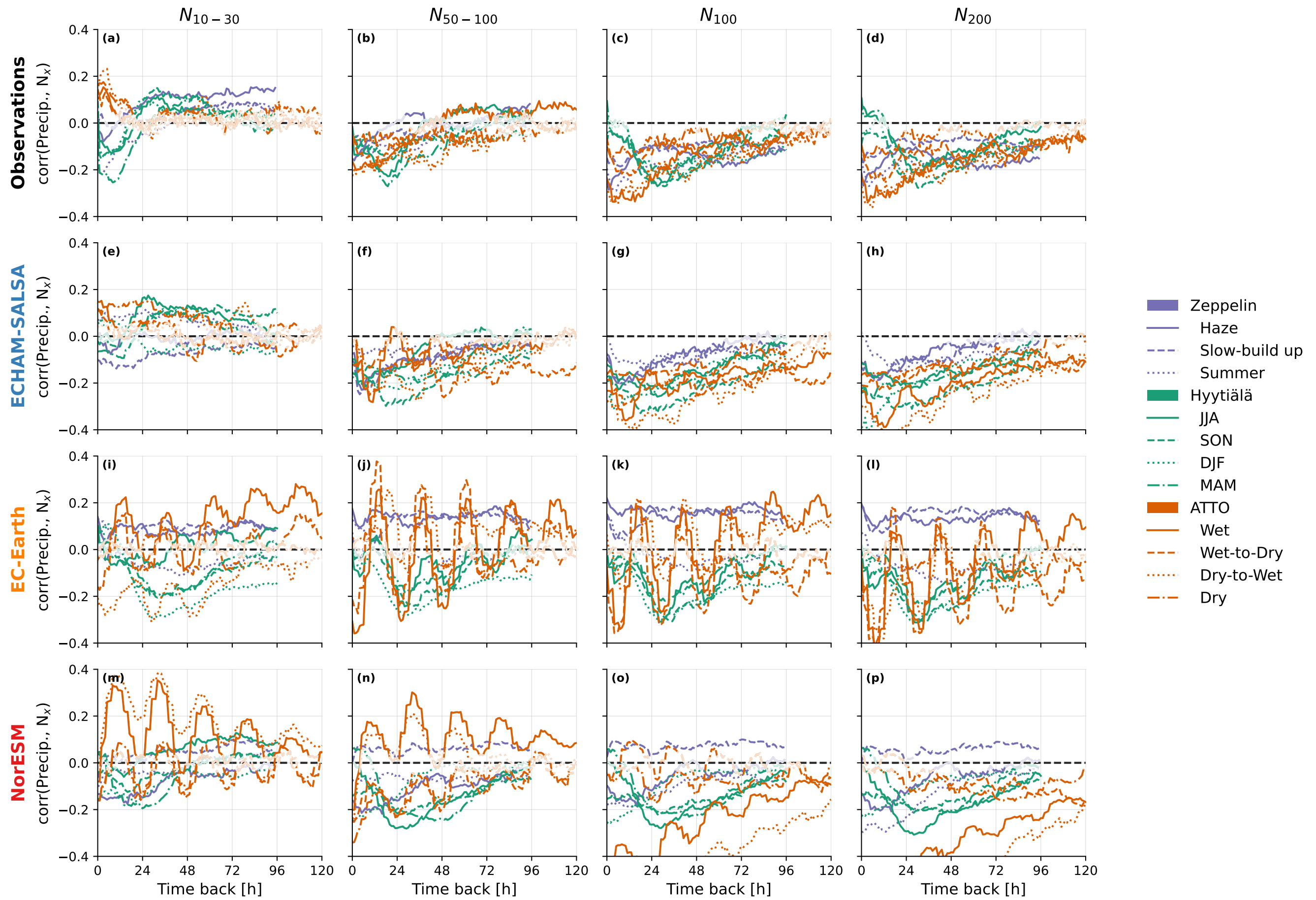

Figure S20. Same as Fig. S19, but with drizzle set to zero below 0.05 $\mathrm{mm/h}$. HYSPLIT data for observations.

Compared to the HYSPLIT output which truncates the values close to zero to absolute zero precipitation, the model have a lot more very low precipitation rates and this impacts the correlations. In Figs. S19 and S20, we show how the correlations look if we use the full model dataset with small values of precipitation included and ERA5 precipitation data for the observations (Fig. S19) and the results when we artificially truncate the model data so that precipitation very close to zero is set to zero (below 0.05 $\mathrm{mm/h}$) and using the truncated HYSPLIT output for the observations (Fig. S19). Mainly they display that the correlations become a little weaker in the models when drizzle is set to zero.

S6 Correlation between precipitation rate and particle number size distritbution

All except ATTO are displayed in the previous section.

S6.1 ATTO

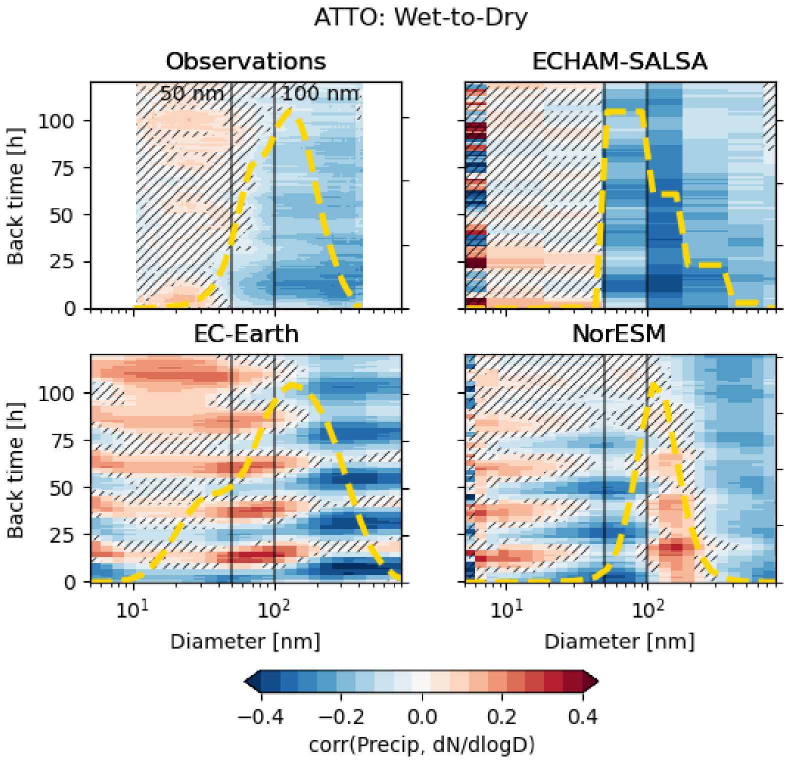

Figure S21. Correlation between rainfall and PNSD, Wet to dry season, ATTO.

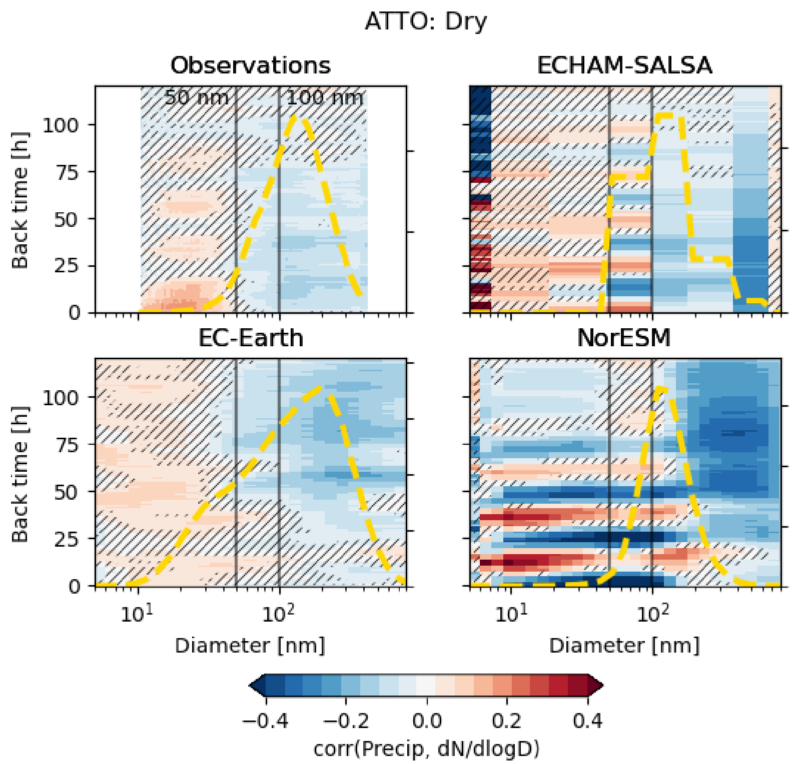

Figure S22. Correlation between rainfall and PNSD, Dry season, ATTO.

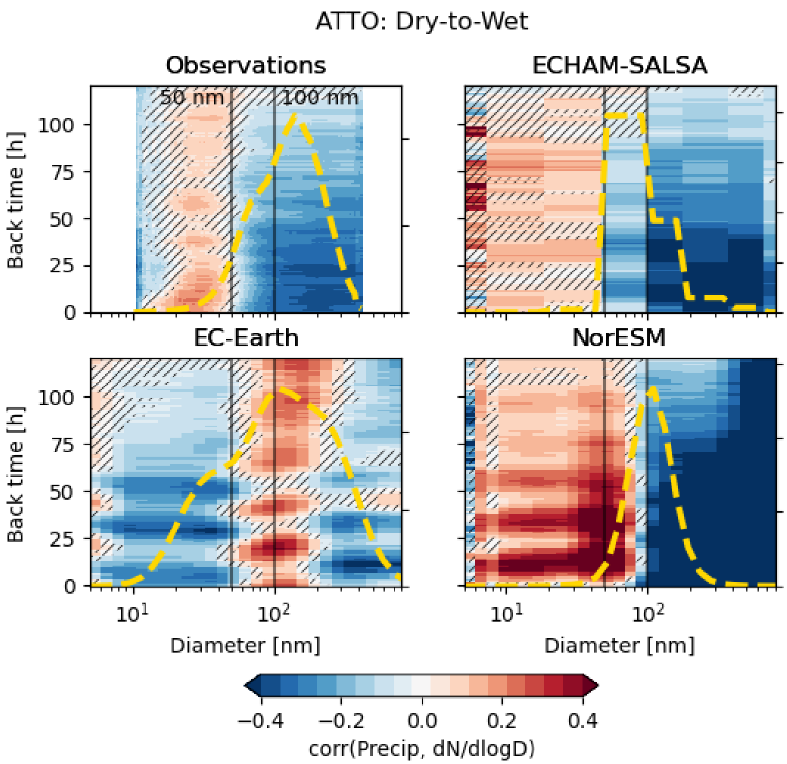

Figure S23. Correlation between rainfall and PNSD, Dry to Wet season, ATTO.

200 **S7 New particle formation**

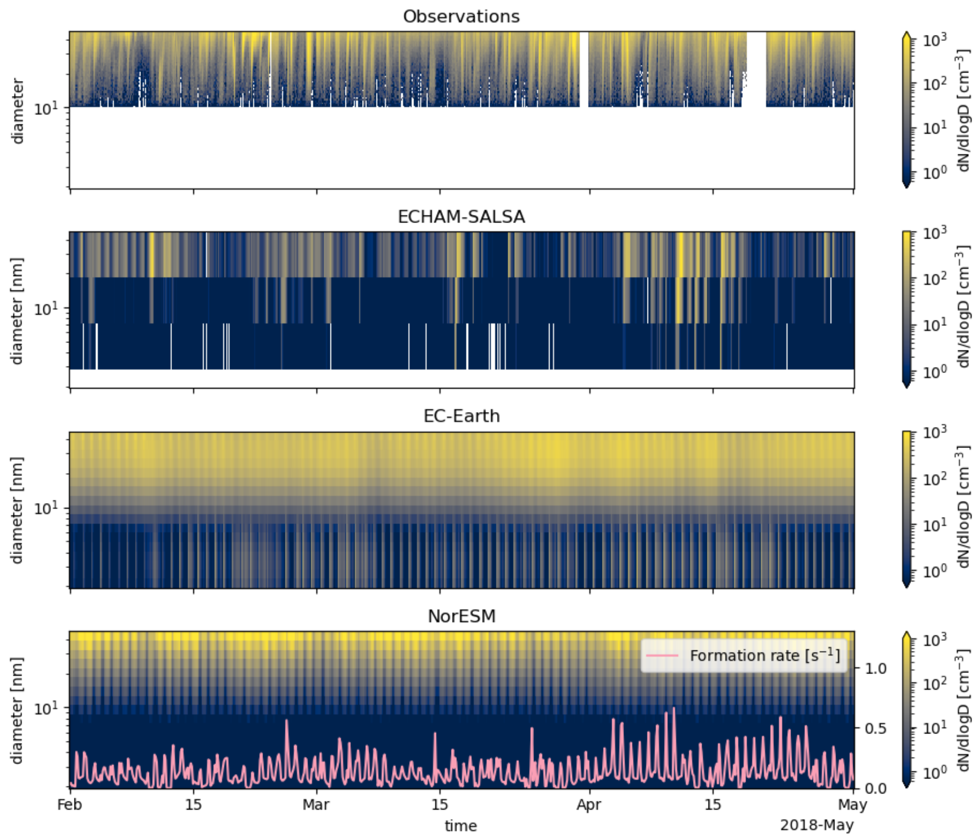

Figure S24. Size distributions in the range 1-50 nm during the wet season (Feb–May) during 2018. For NorESM the formation rate of particles is also shown.

S8 Trajectories

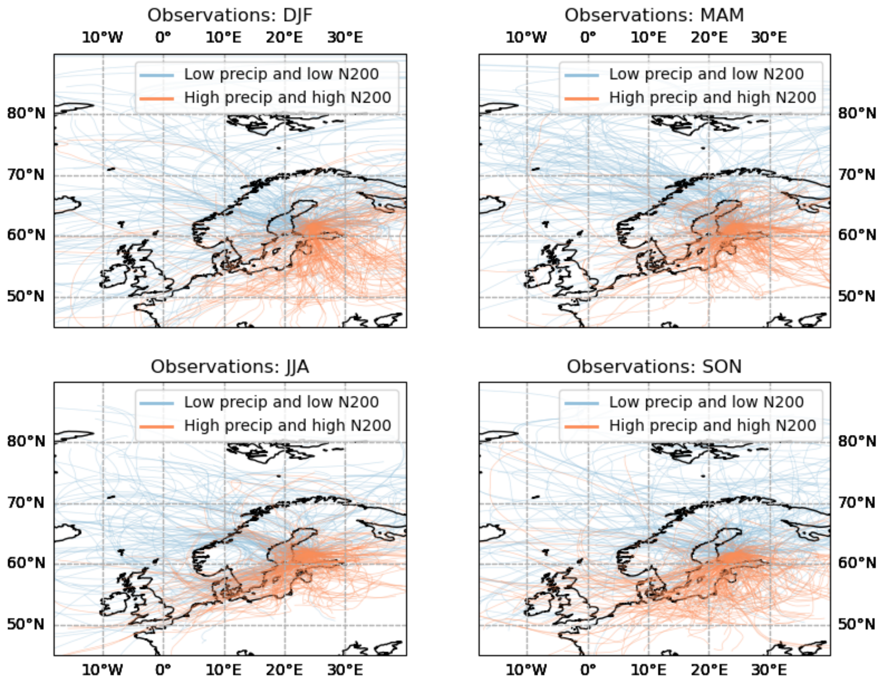

Figure S25. Trajectories for low recent precipitation and low N_{200} (blue, defined as below/above the mean) and high recent precipitation and high N_{200} (orange). Recent precipitation is calculated as the average of the last 18 hours before the airmass arrival at the station. A random sample of 200 trajectories are plotted for each group.

S9 Correlation in different sectors for Hyytiälä

Note that these results use GDAS data for "observed" precipitation.

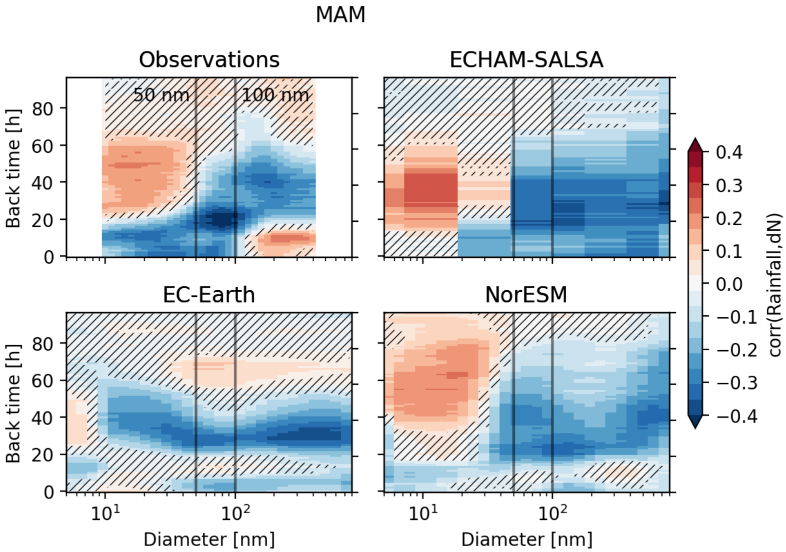

Figure S26. The Spearmann correlation between size distribution measured or modelled at the station and precipitation along the trajectory to the station when only trajectories in sector -175 to 5 degrees centered at the station are taken into account, assuming 0 degrees is straight east.

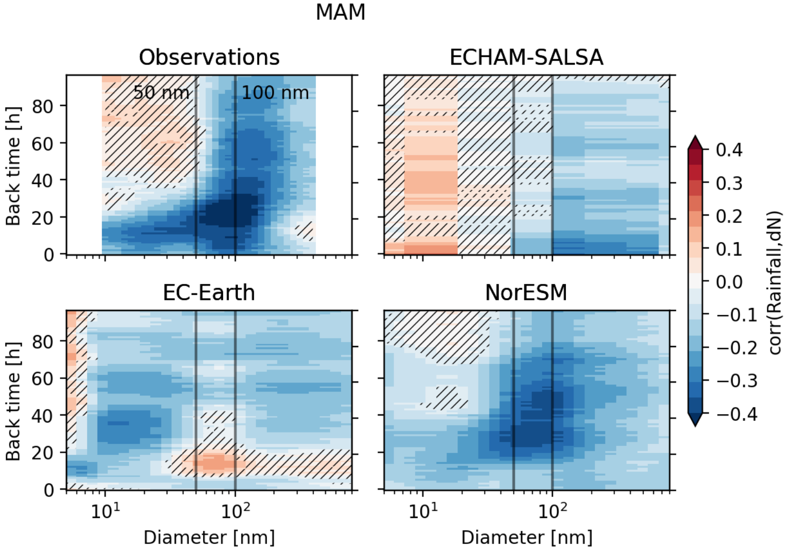

Figure S27. The Spearmann correlation between size distribution measured or modelled at the station and precipitation along the trajectory to the station when only trajectories in sector 5 to 185 degrees centered at the station are taken into account, assuming 0 degrees is straight east.

S10 Correlation between precipitation rate and particle number size distritbution calculated based on daily means

205 ### S10.1 Hyytiälä

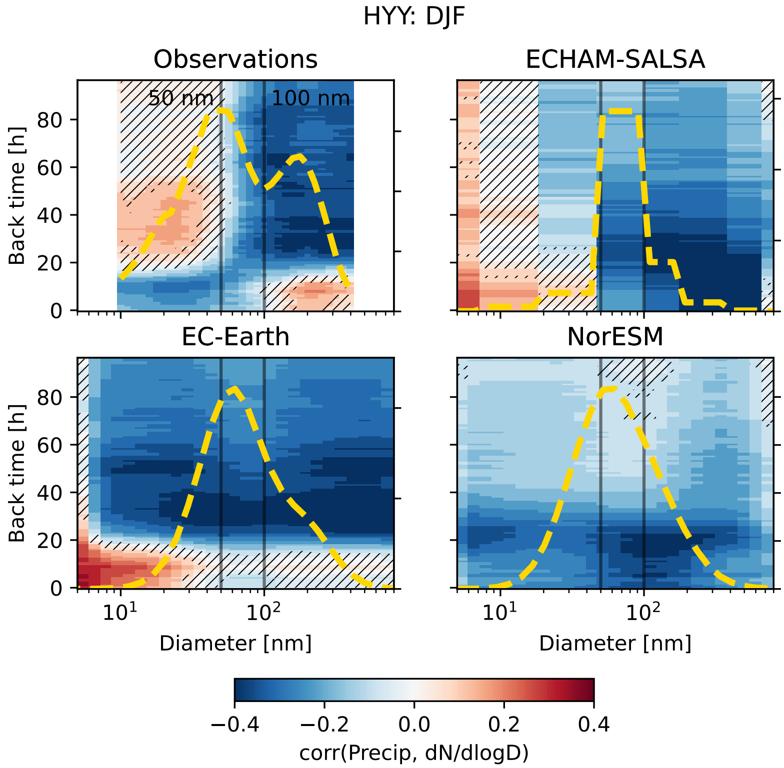

Figure S28. Correlation between rainfall and PNSD, DJF, Hyytiälä, calculated based on daily mean values.

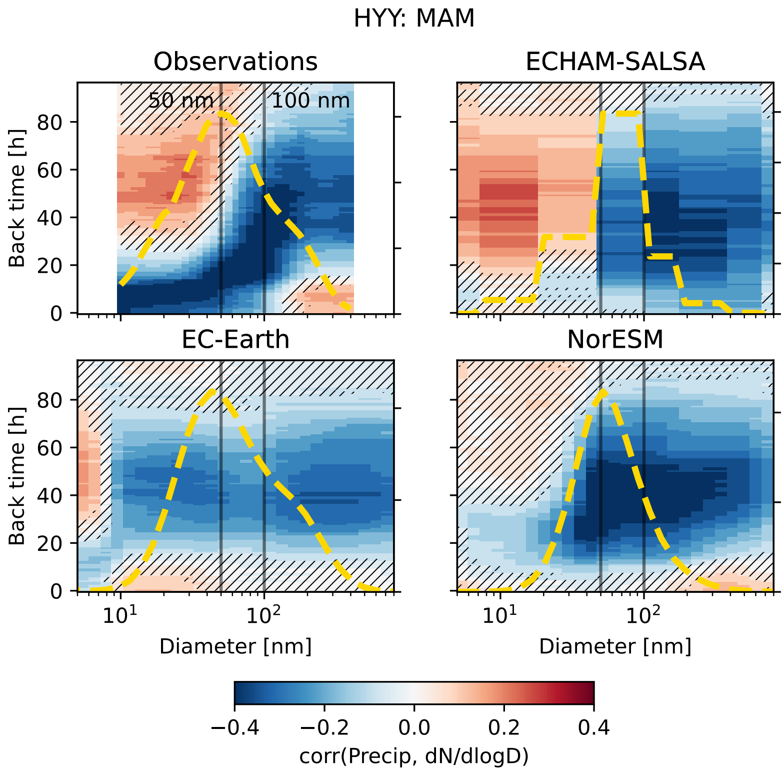

Figure S29. Correlation between rainfall and PNSD, MAM, Hyytiälä, calculated based on daily mean values.

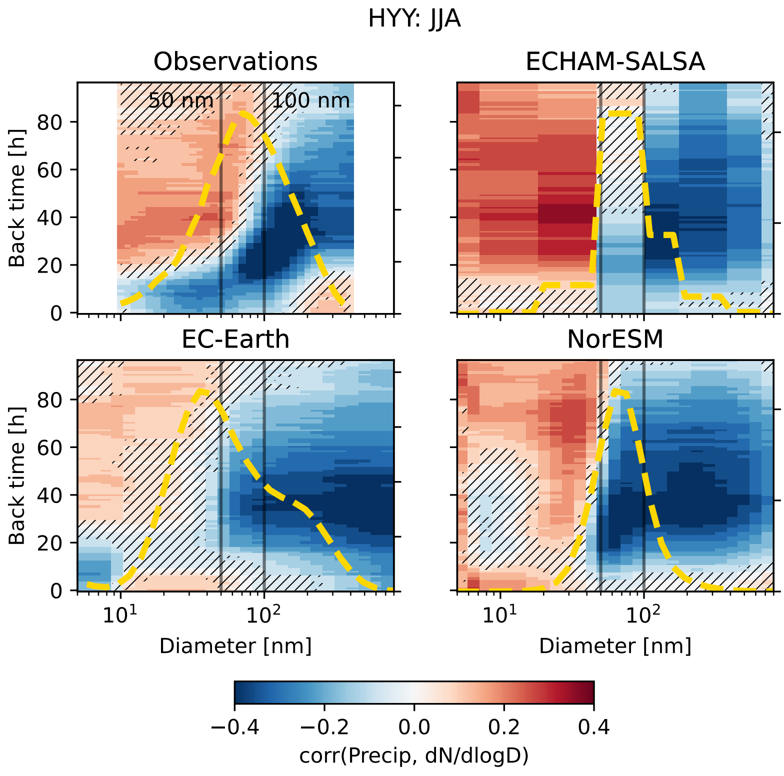

Figure S30. Correlation between rainfall and PNSD, JJA, Hyytiälä, calculated based on daily mean values.

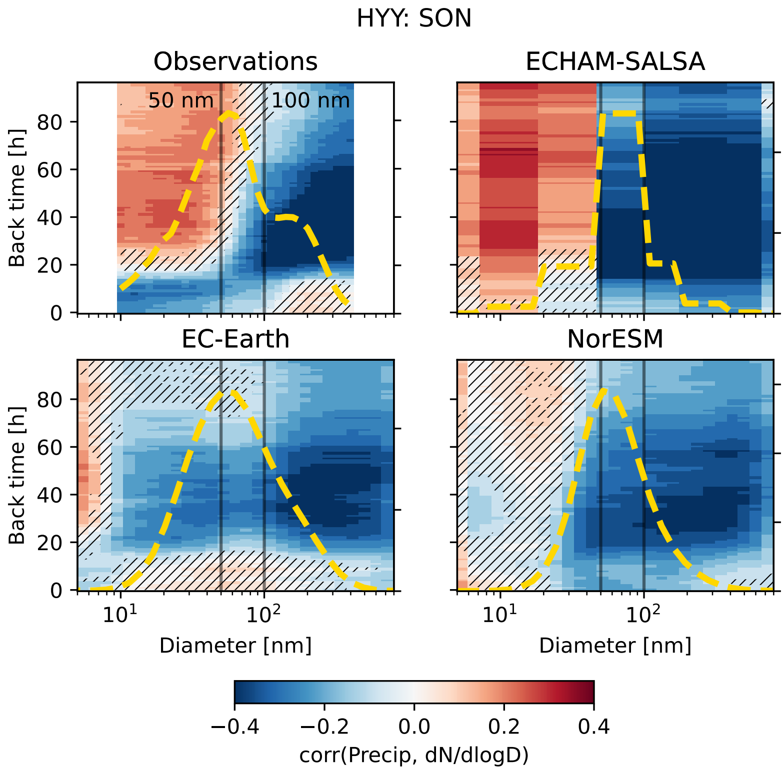

Figure S31. Correlation between rainfall and PNSD, SON, Hyytiälä, calculated based on daily mean values.

S10.2 Zeppelin

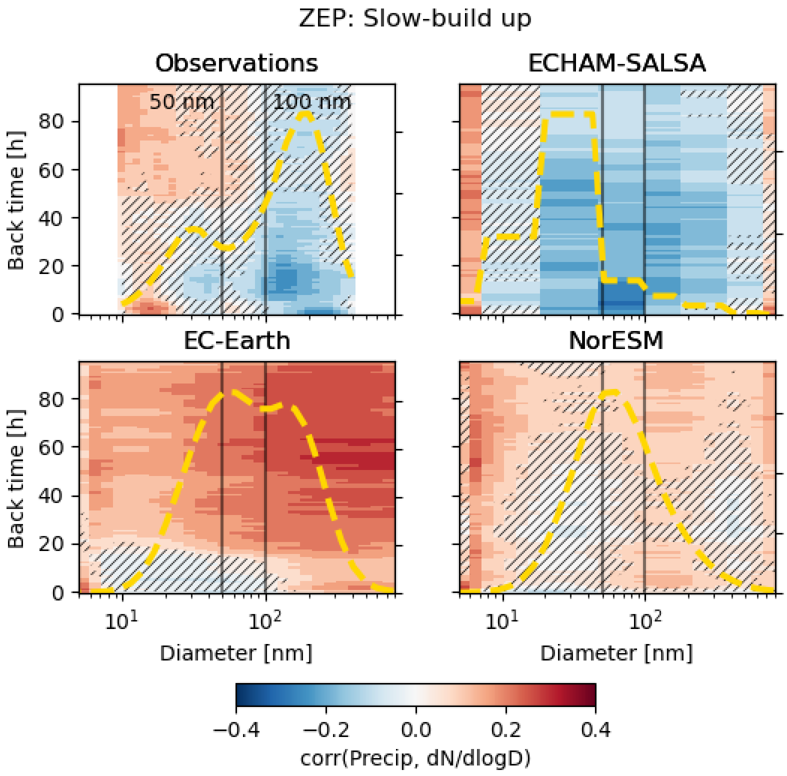

Figure S32. Correlation between rainfall and PNSD, Slow build up, Zeppelin, calculated based on daily mean values.

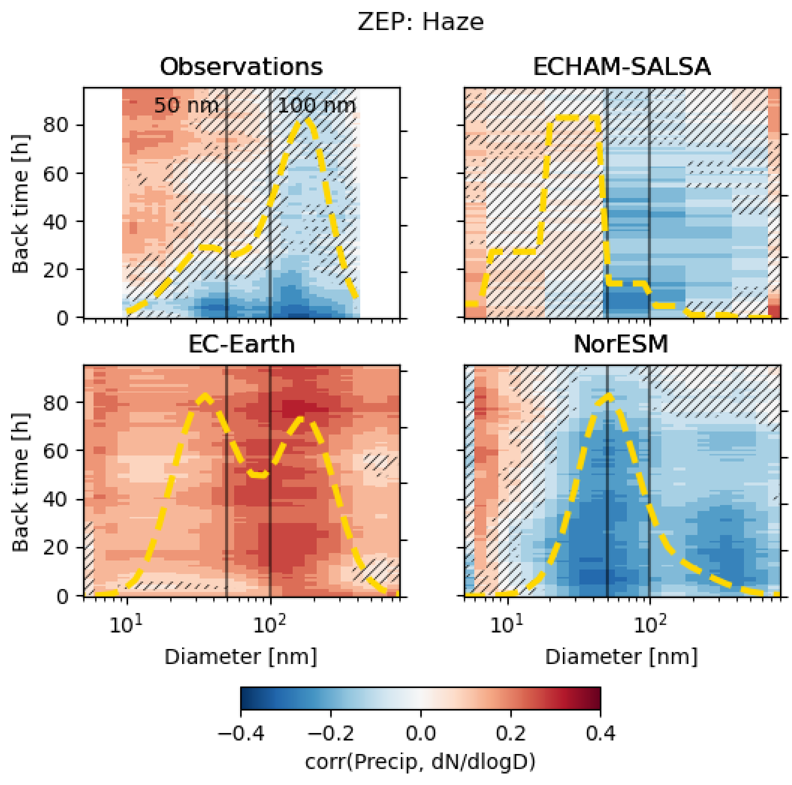

Figure S33. Correlation between rainfall and PNSD, Haze, Zeppelin, calculated based on daily mean values.

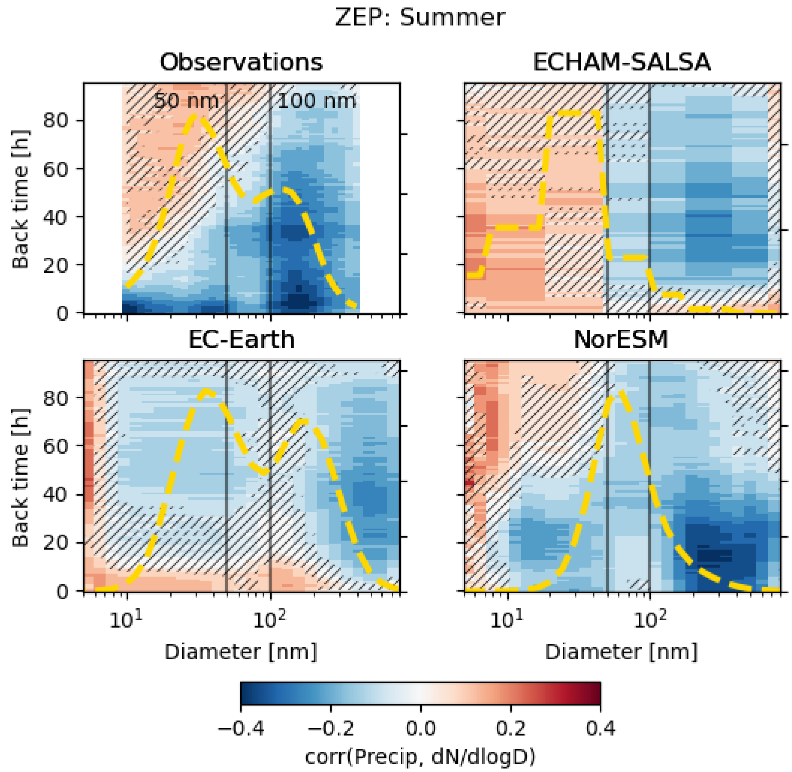

Figure S34. Correlation between rainfall and PNSD, Summer, Zeppelin, calculated based on daily mean values.

S10.3 ATTO

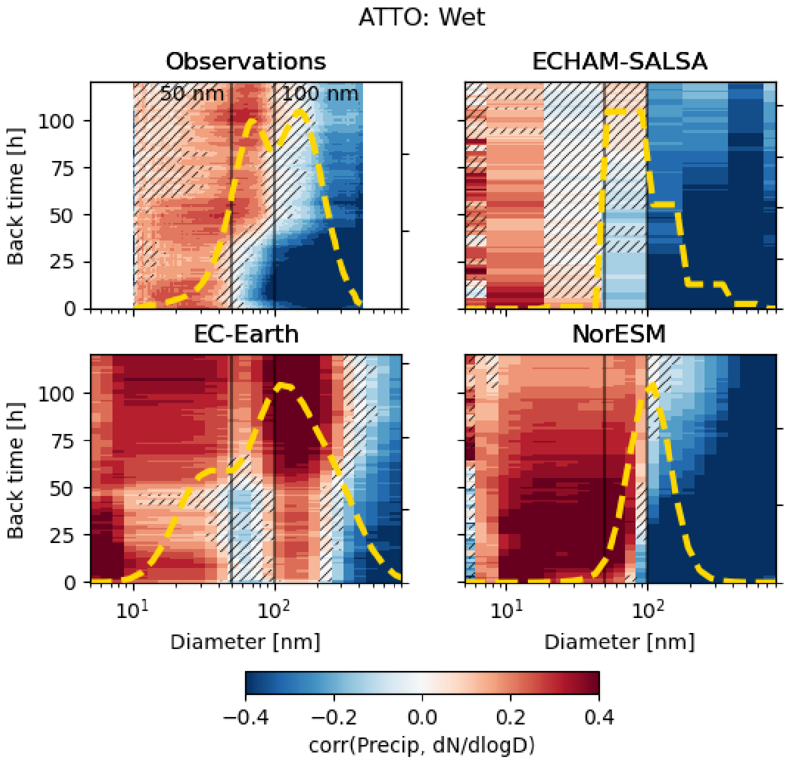

Figure S35. Correlation between rainfall and PNSD, Wet season, ATTO, calculated based on daily mean values.

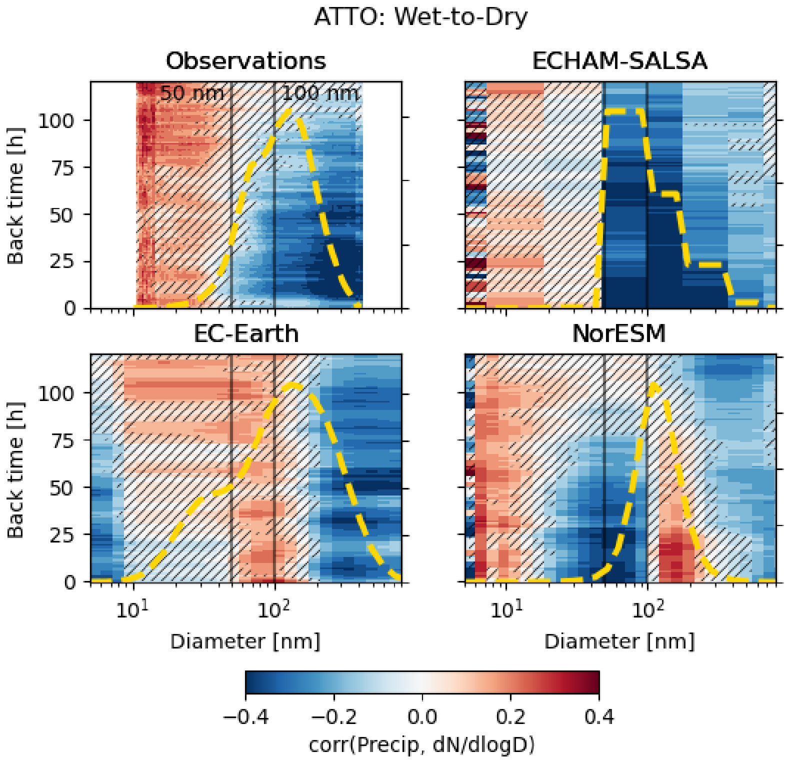

Figure S36. Correlation between rainfall and PNSD, Wet-to-Dry season, ATTO, calculated based on daily mean values.

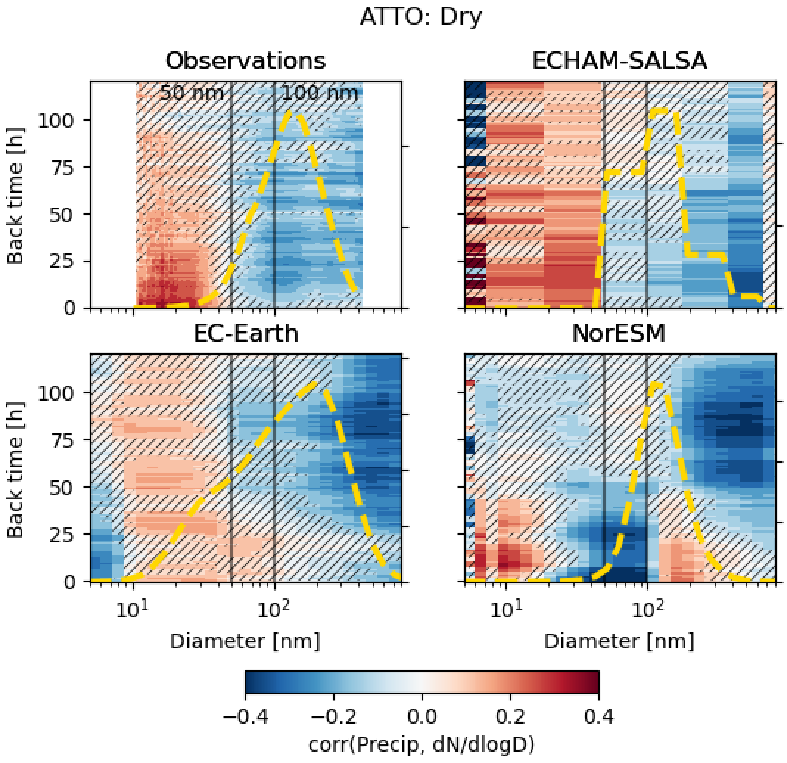

Figure S37. Correlation between rainfall and PNSD, Dry season, ATTO, calculated based on daily mean values.

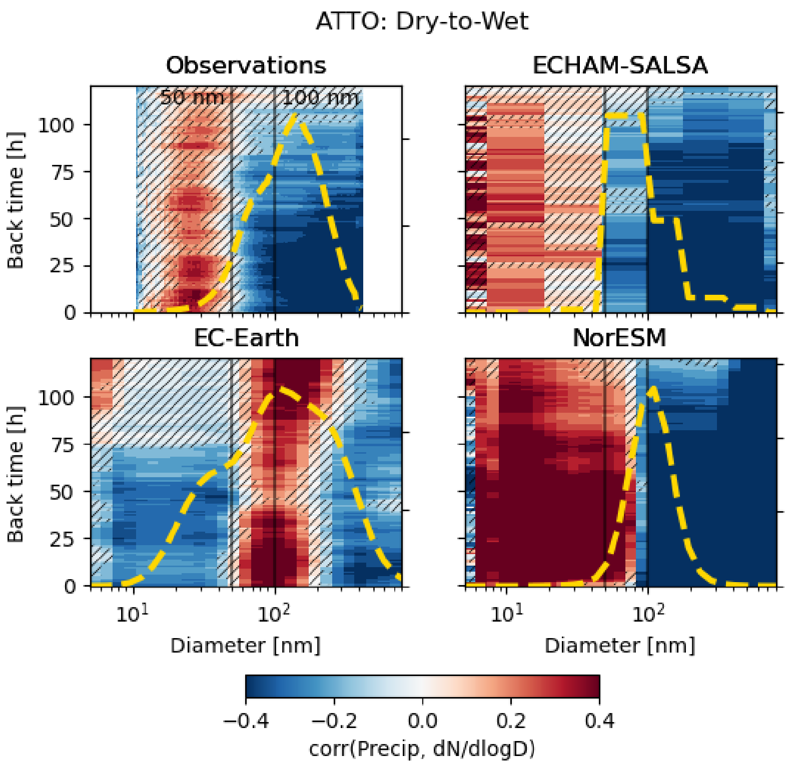

Figure S38. Correlation between rainfall and PNSD, Dry-to-Wet season, ATTO, calculated based on daily mean values.

S11 XGBoost

S11.1 XGBoost evaluation

210 In the plots below, we have used all except the last year (2018) for training of the XGBoost, keeping the other parameters the same as in the main text (see the methods section). The results are thus for predictions for the testing year 2018.

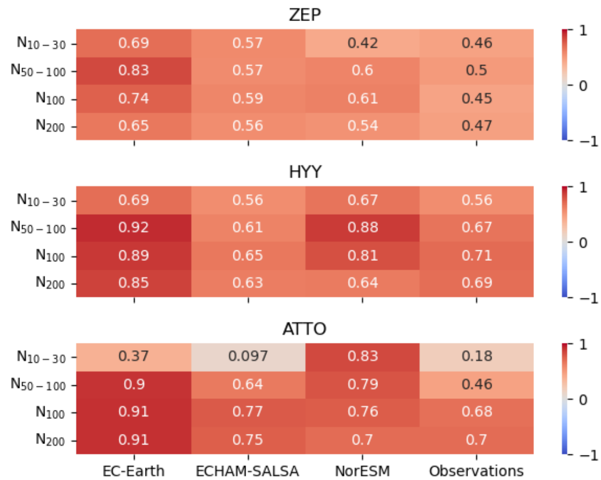

Figure S39. Pearson correlation coefficients for XGBoost modelled results versus observed results for 2018 for each station and size interval.

S11.1.1 Zeppelin

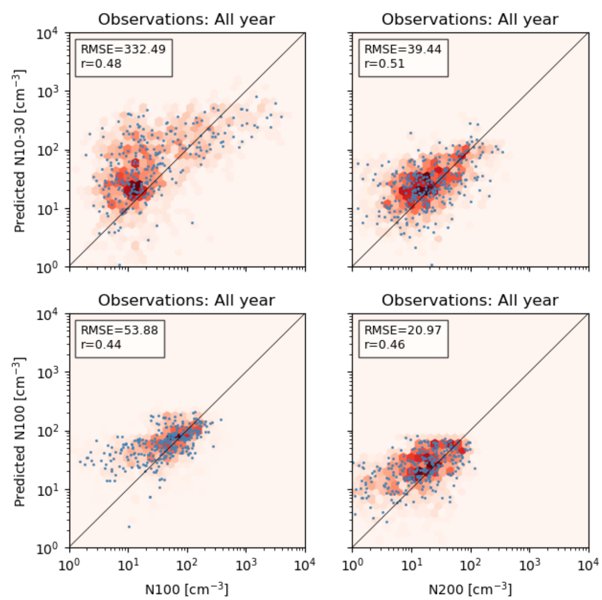

Figure S40. Evaluation of XGBoost model for Zeppelin station and observations/reanalysis.

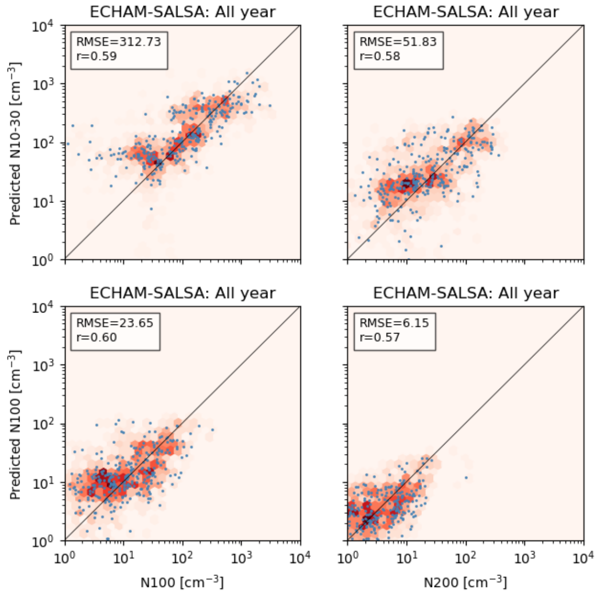

Figure S41. Evaluation of XGBoost model for Zeppelin station and ECHAM-SALSA.

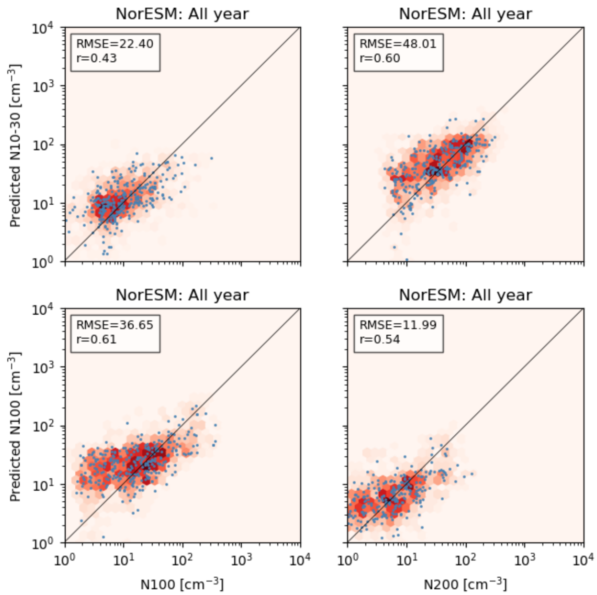

Figure S42. Evaluation of XGBoost model for Zeppelin station and NorESM.

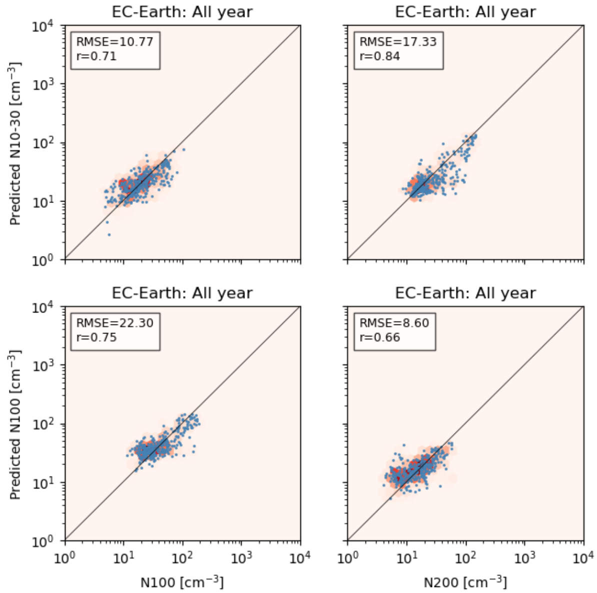

Figure S43. Evaluation of XGBoost model for Zeppelin station and EC-Earth.

S11.1.2 Hyytiälä

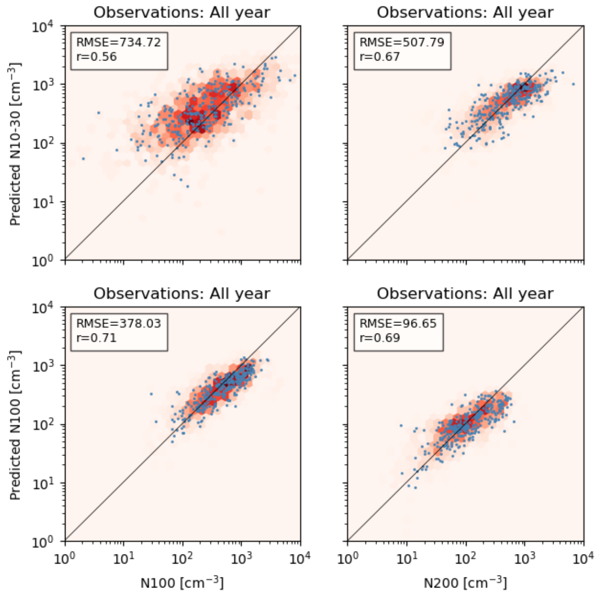

Figure S44. Evaluation of XGBoost model for Hyytiälä station and observations/reanalysis.

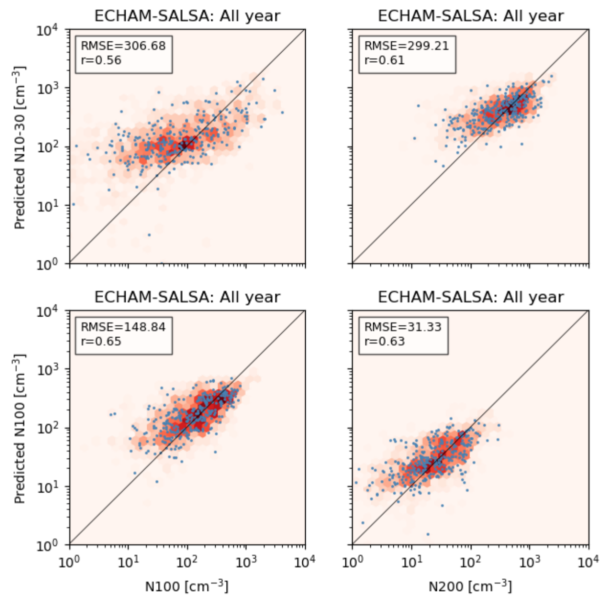

Figure S45. Evaluation of XGBoost model for Zeppelin station and ECHAM-SALSA.

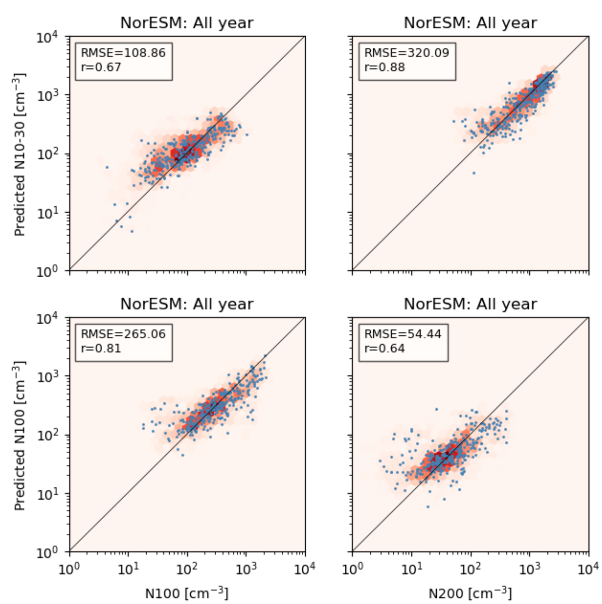

Figure S46. Evaluation of XGBoost model for Hyytiälä station and NorESM.

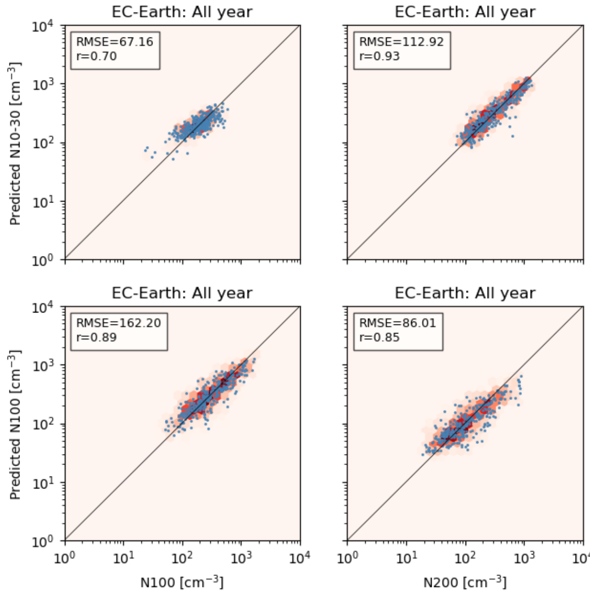

Figure S47. Evaluation of XGBoost model for Hyytiälä station and EC-Earth.

S11.1.3 ATTO

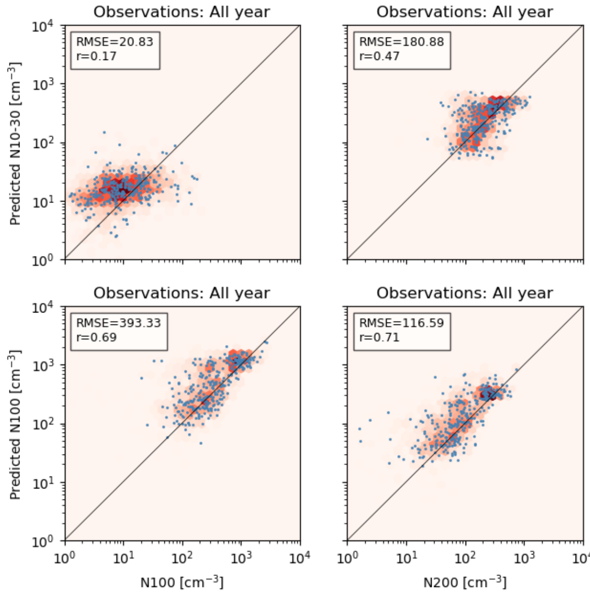

Figure S48. Evaluation of XGBoost model for ATTO station and observations/reanalysis.

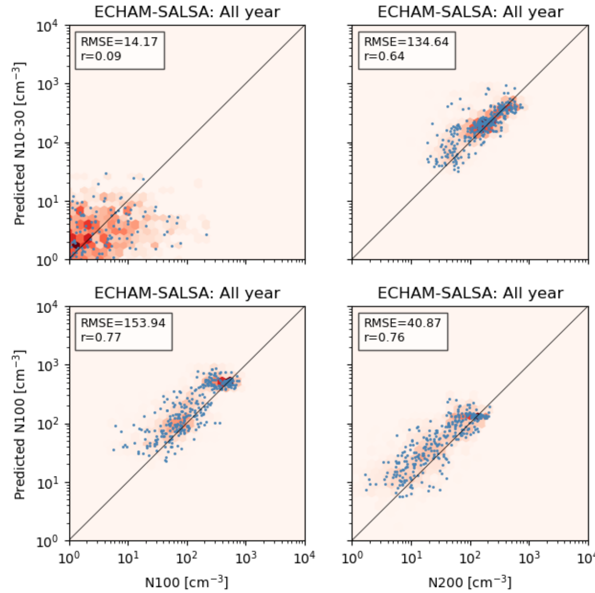

Figure S49. Evaluation of XGBoost model for ATTO station and ECHAM-SALSA.

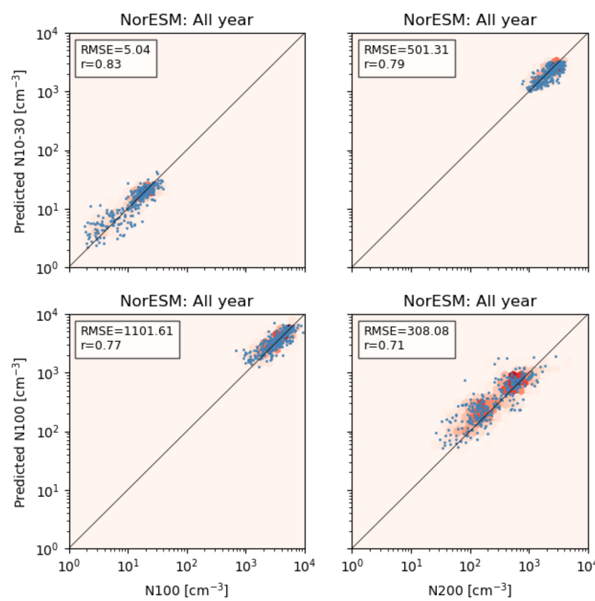

Figure S50. Evaluation of XGBoost model for ATTO station and NorESM.

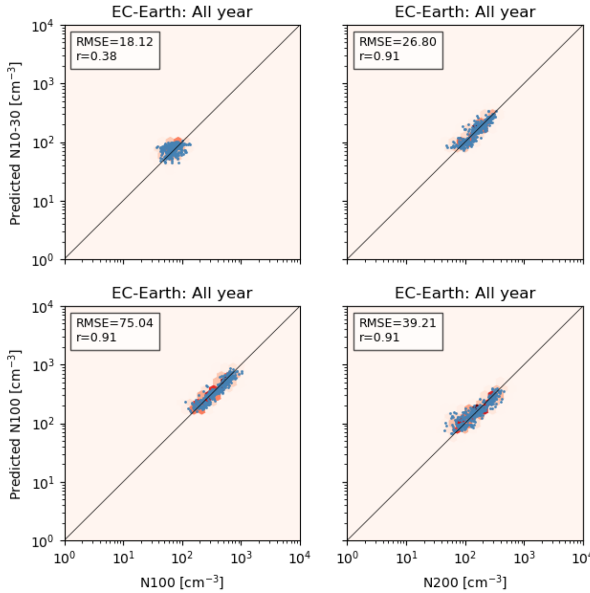

Figure S51. Evaluation of XGBoost model for ATTO station and EC-Earth.

S11.2 XGBoost SHAP values

SHAP (SHapley Additive exPlanations) values are a method from game theory used to explain the output of machine learning models. They quantify how much each input feature contributes to a specific prediction. In the below, we present SHAP value analysis for the XGBoost regressions created for the analysis in the manuscript.

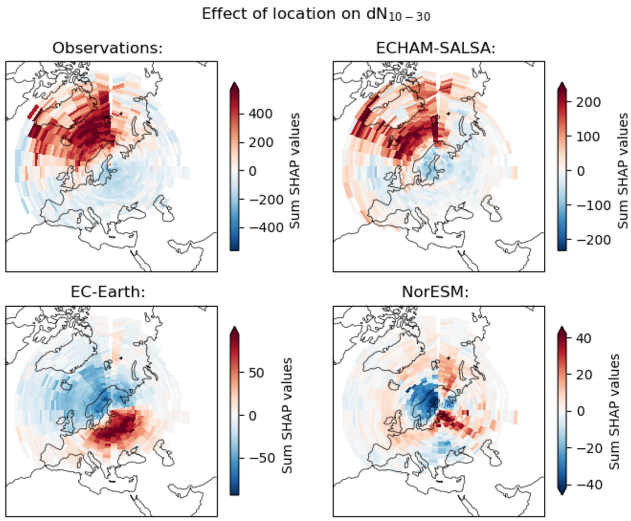

Figure S52. These maps show the "impact" in terms of SHAP values of a trajectory passing through each of grid cells on its way to the station on N_{10-30} for Hyyitälä station. The sum of the SHAP values for all trajectories passings through that grid box is calculated (independent of when before arriving at the station), and finally the average of these sums is calculated (over the time dimension).

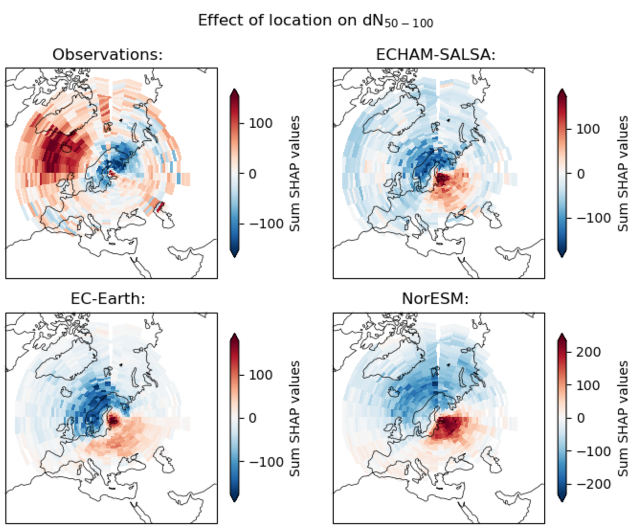

Figure S53. These maps show the "impact" in terms of SHAP values of a trajectory passing through each of grid cells on its way to the station on N_{50-100} for Hyyitälä station. Please see caption of Fig. S52 for description of the calculation.

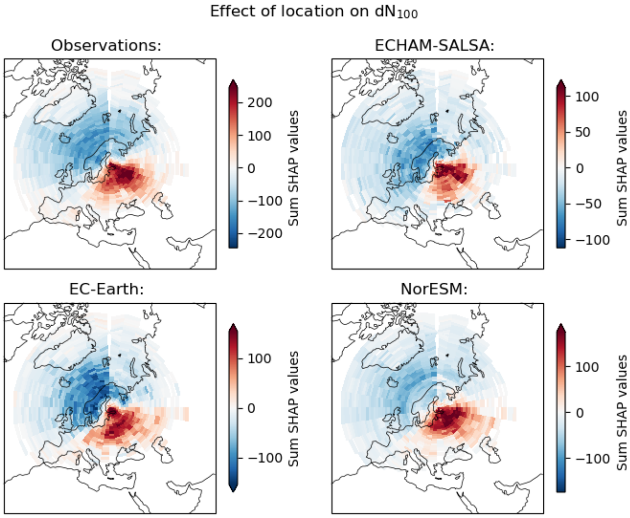

Figure S54. These maps show the "impact" in terms of SHAP values of a trajectory passing through each of grid cells on its way to the station on N_{100} for Hyyitälä station. Please see caption of Fig. S52 for description of the calculation.

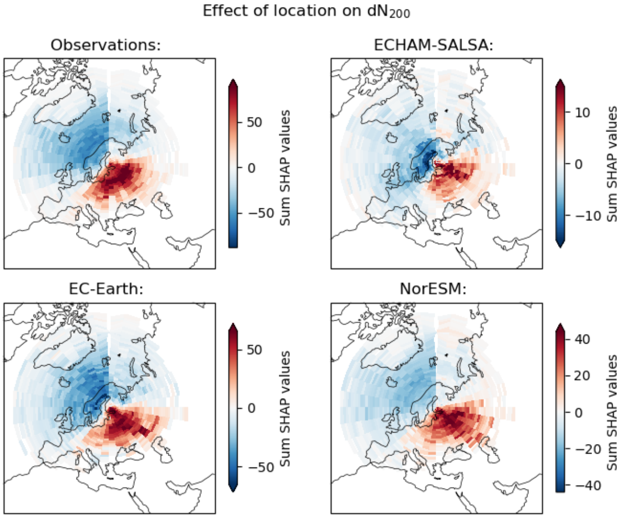

Figure S55. These maps show the "impact" in terms of SHAP values of a trajectory passing through each of grid cells on its way to the station on N_{200} for Hyyitälä station. Please see caption of Fig. S52 for description of the calculation.

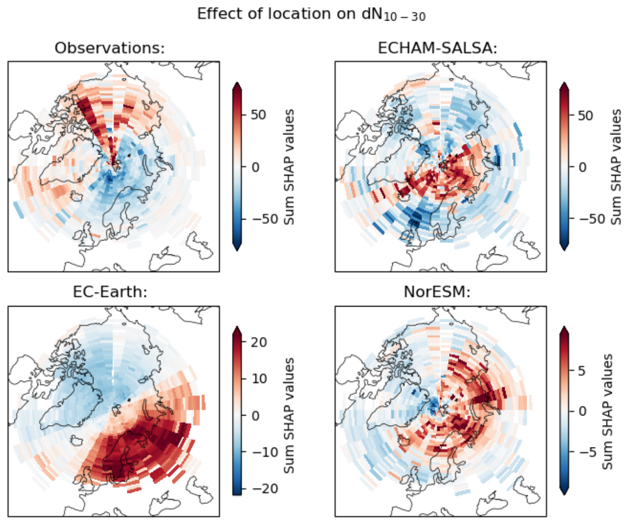

Figure S56. These maps show the "impact" in terms of SHAP values of a trajectory passing through each of grid cells on its way to the station on N_{10-30} for Zeppelin station. Please see caption of Fig. S52 for description of the calculation.

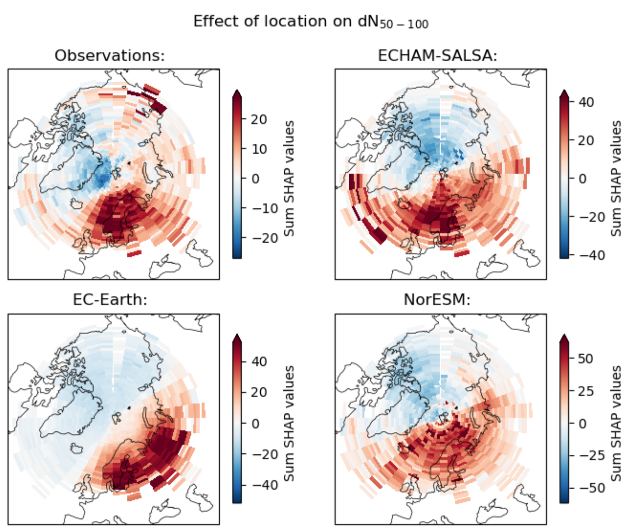

Figure S57. These maps show the "impact" in terms of SHAP values of a trajectory passing through each of grid cells on its way to the station on N_{50-100} for Zeppelin station. Please see caption of Fig. S52 for description of the calculation.

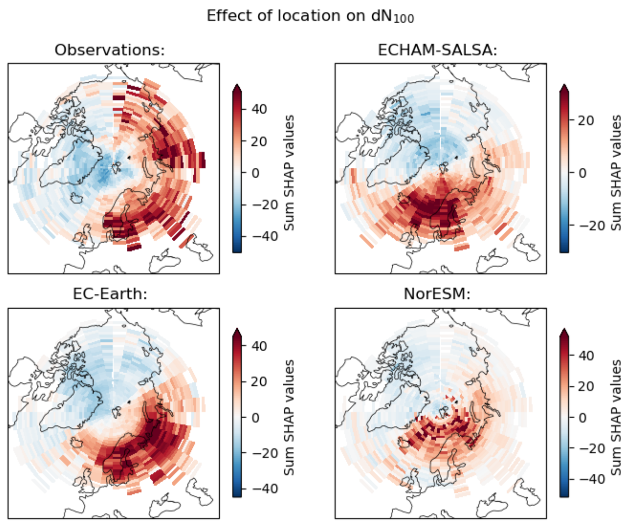

Figure S58. These maps show the "impact" in terms of SHAP values of a trajectory passing through each of grid cells on its way to the station on N_{100} for Zeppelin station. Please see caption of Fig. S52 for description of the calculation.

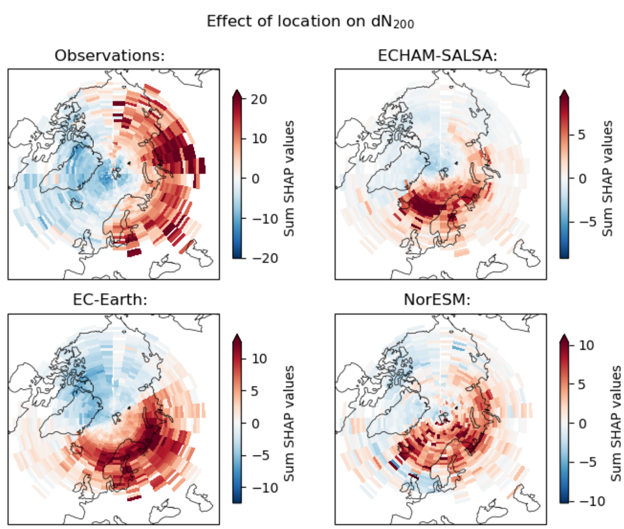

Figure S59. These maps show the "impact" in terms of SHAP values of a trajectory passing through each of grid cells on its way to the station on N_{200} for Zeppelin station. Please see caption of Fig. S52 for description of the calculation.

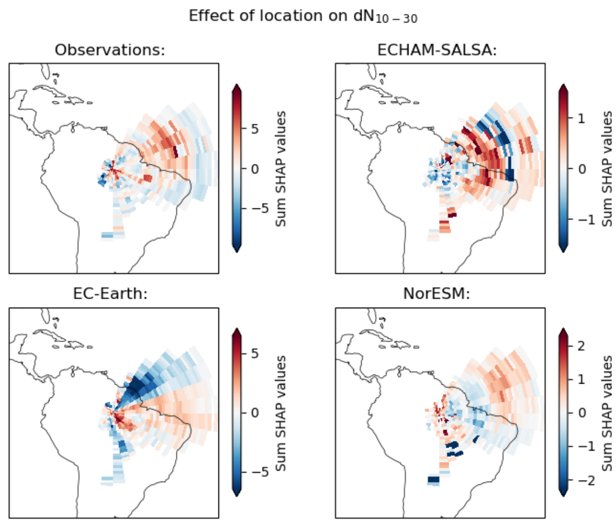

Figure S60. These maps show the "impact" in terms of SHAP values of a trajectory passing through each of grid cells on its way to the station on N_{10-30} for ATTO station. Please see caption of Fig. S52 for description of the calculation.

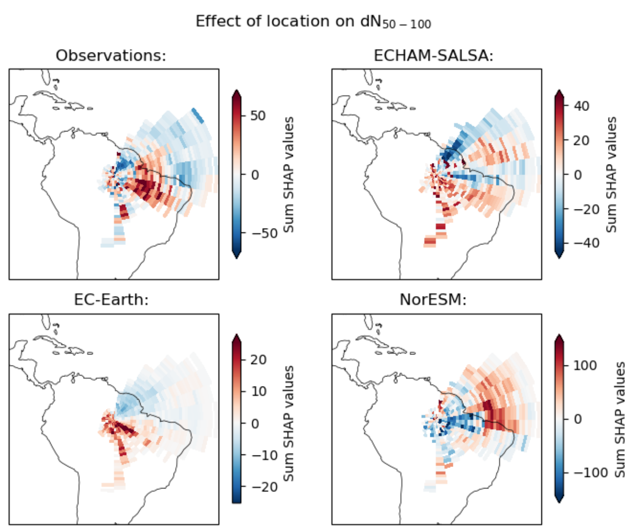

Figure S61. These maps show the "impact" in terms of SHAP values of a trajectory passing through each of grid cells on its way to the station on N_{50-100} for ATTO station. Please see caption of Fig. S52 for description of the calculation.

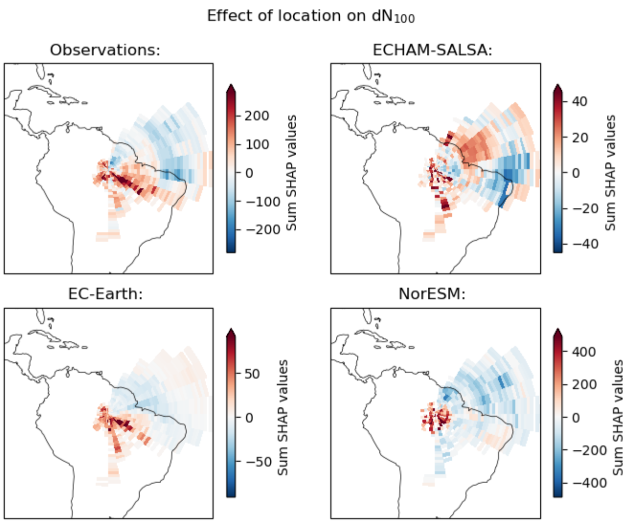

Figure S62. These maps show the "impact" in terms of SHAP values of a trajectory passing through each of grid cells on its way to the station on N_{100} for ATTO station. Please see caption of Fig. S52 for description of the calculation.

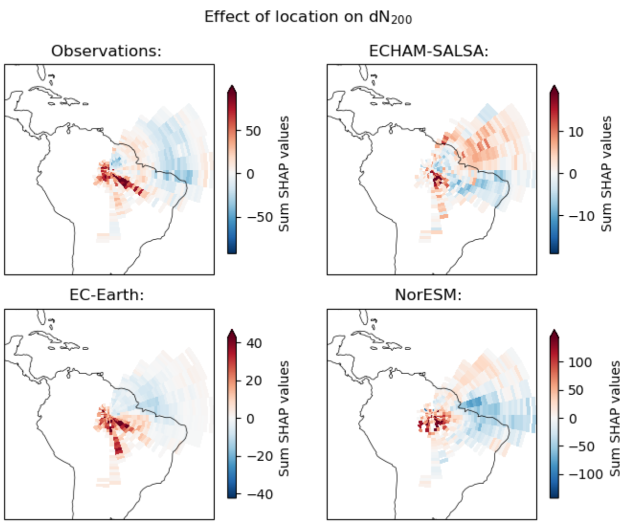

Figure S63. These maps show the "impact" in terms of SHAP values of a trajectory passing through each of grid cells on its way to the station on N_{200} for ATTO station. Please see caption of Fig. S52 for description of the calculation.

S11.3 SHAP values for recent (6h) precipitation

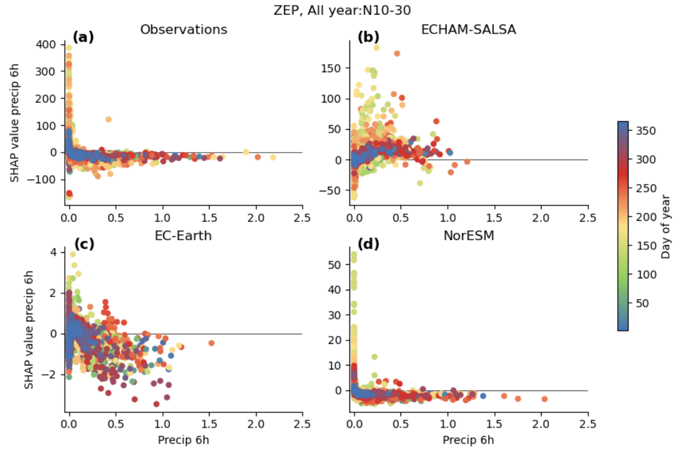

Figure S64. Zeppelin: Scatter plots showing the SHAP values for of the first 6h average precipitation rate prior to the airmass reaching the station for predicting N_{10-30}. The color indicated the day of the year.

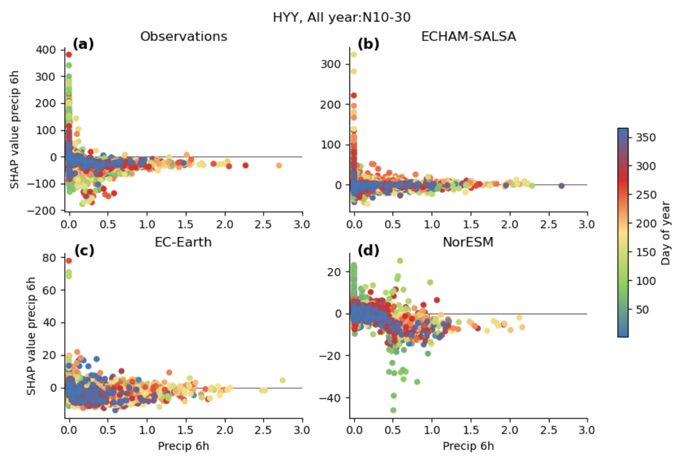

Figure S65. Hyytiälä: Scatter plots showing the SHAP values for of the first 6h average precipitation rate prior to the airmass reaching the station for predicting N_{10-30}. The color indicated the day of the year.

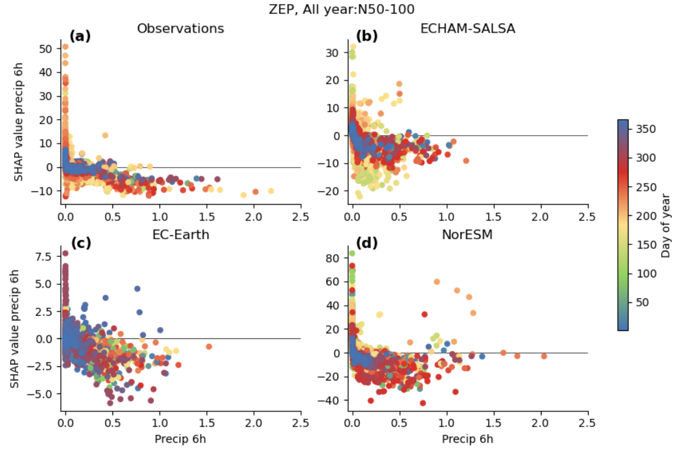

Figure S66. Zeppelin: Scatter plots showing the SHAP values for of the first 6h average precipitation rate prior to the airmass reaching the station for predicting N_{50-100}. The color indicated the day of the year.

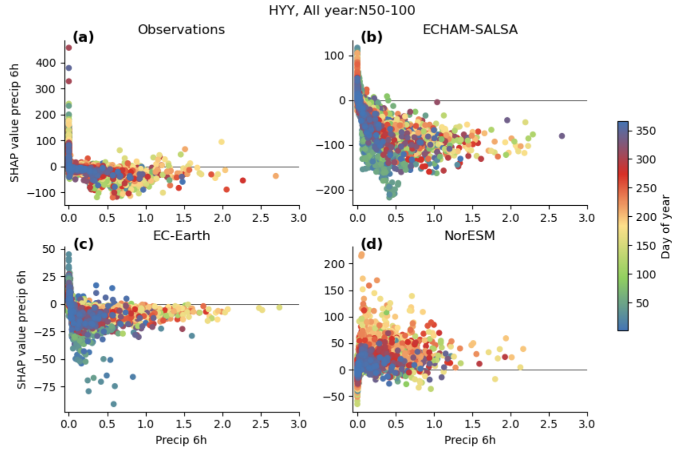

Figure S67. Hyytiälä: Scatter plots showing the SHAP values for of the first 6h average precipitation rate prior to the airmass reaching the station for predicting N_{50-100}. The color indicated the day of the year.

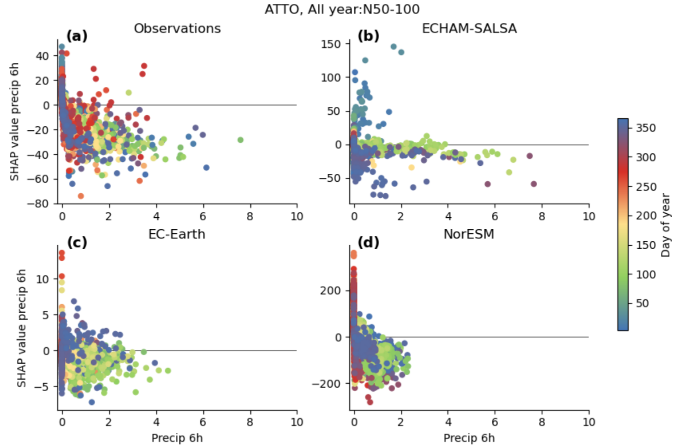

Figure S68. ATTO: Scatter plots showing the SHAP values for of the first 6h average precipitation rate prior to the airmass reaching the station for predicting N_{50-100}. The color indicated the day of the year.

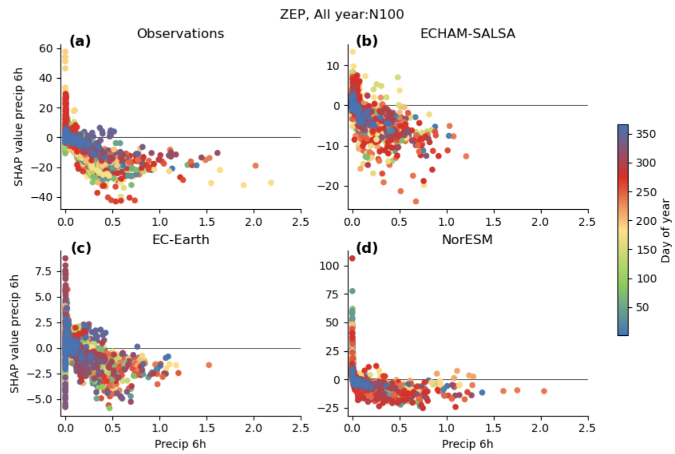

Figure S69. Zeppelin: Scatter plots showing the SHAP values for of the first 6h average precipitation rate prior to the airmass reaching the station for predicting N_{100}. The color indicated the day of the year.

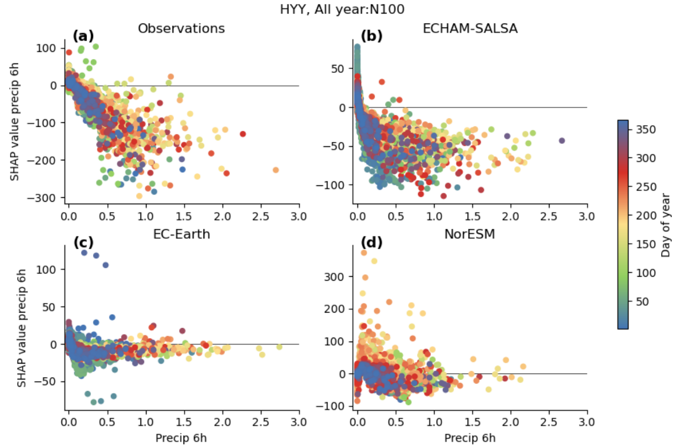

Figure S70. Hyytiälä: Scatter plots showing the SHAP values for of the first 6h average precipitation rate prior to the airmass reaching the station for predicting N_{100}. The color indicated the day of the year.

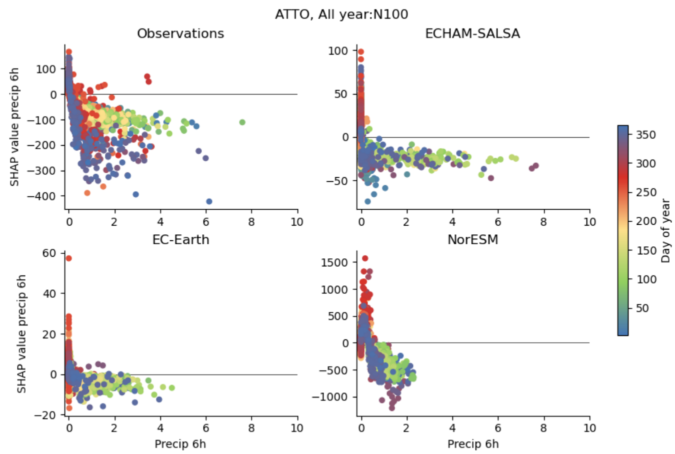

Figure S71. ATTO: Scatter plots showing the SHAP values for of the first 6h average precipitation rate prior to the airmass reaching the station for predicting N_{100}. The color indicated the day of the year.

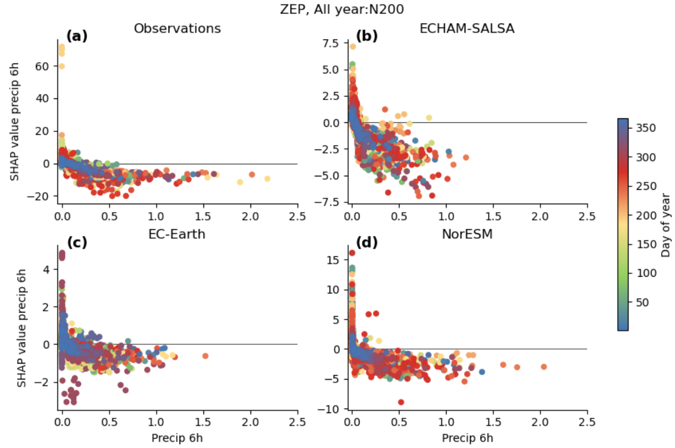

Figure S72. Zeppelin: Scatter plots showing the SHAP values for of the first 6h average precipitation rate prior to the airmass reaching the station for predicting N_{200}. The color indicated the day of the year.

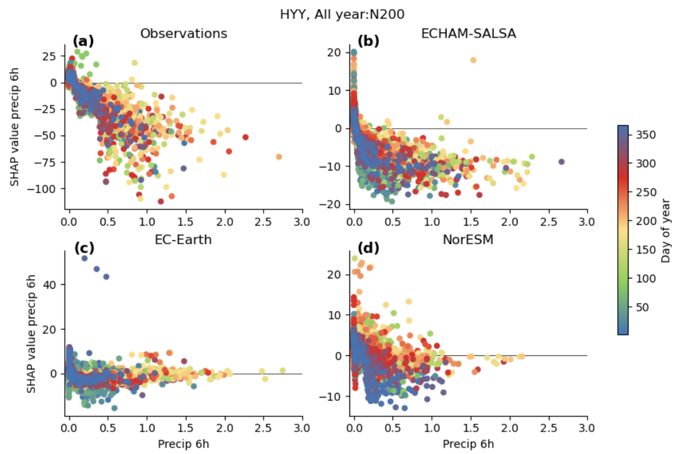

Figure S73. Hyytiälä: Scatter plots showing the SHAP values for of the first 6h average precipitation rate prior to the airmass reaching the station for predicting N_{200}. The color indicated the day of the year.

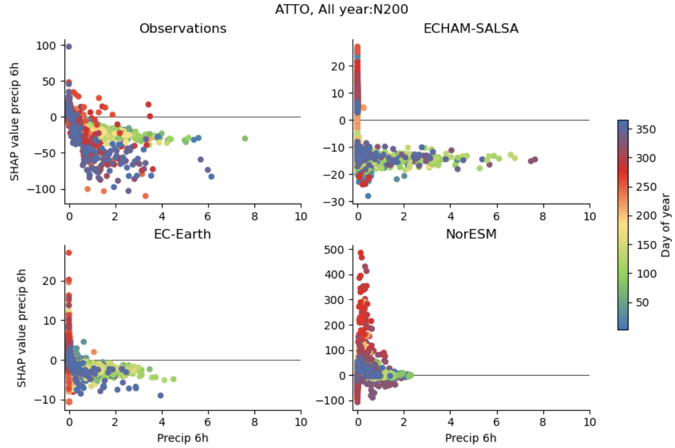

Figure S74. ATTO: Scatter plots showing the SHAP values for of the first 6h average precipitation rate prior to the airmass reaching the station for predicting N_{200}. The color indicated the day of the year.

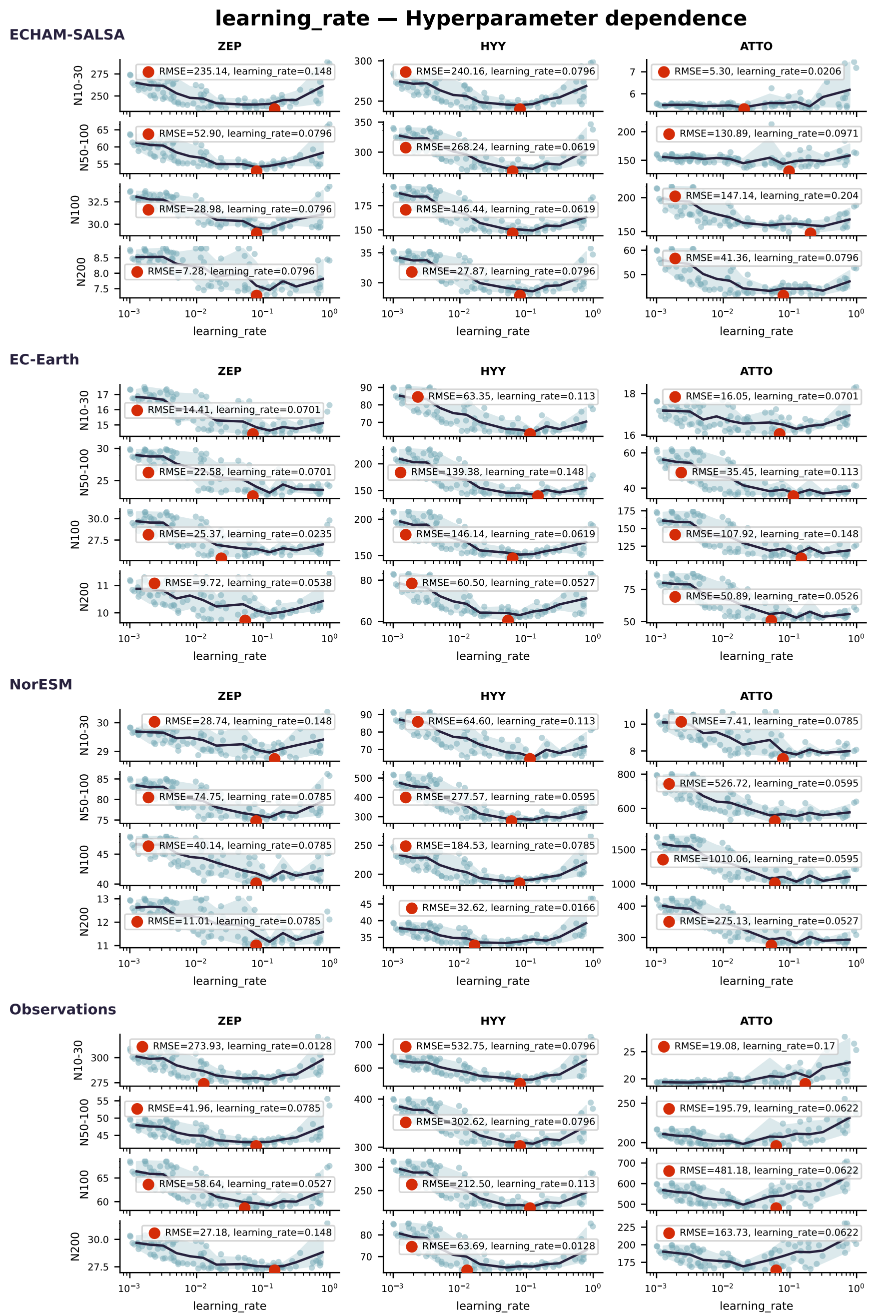

Figure S75. Parameter tuning for XGBoost for learning rate.

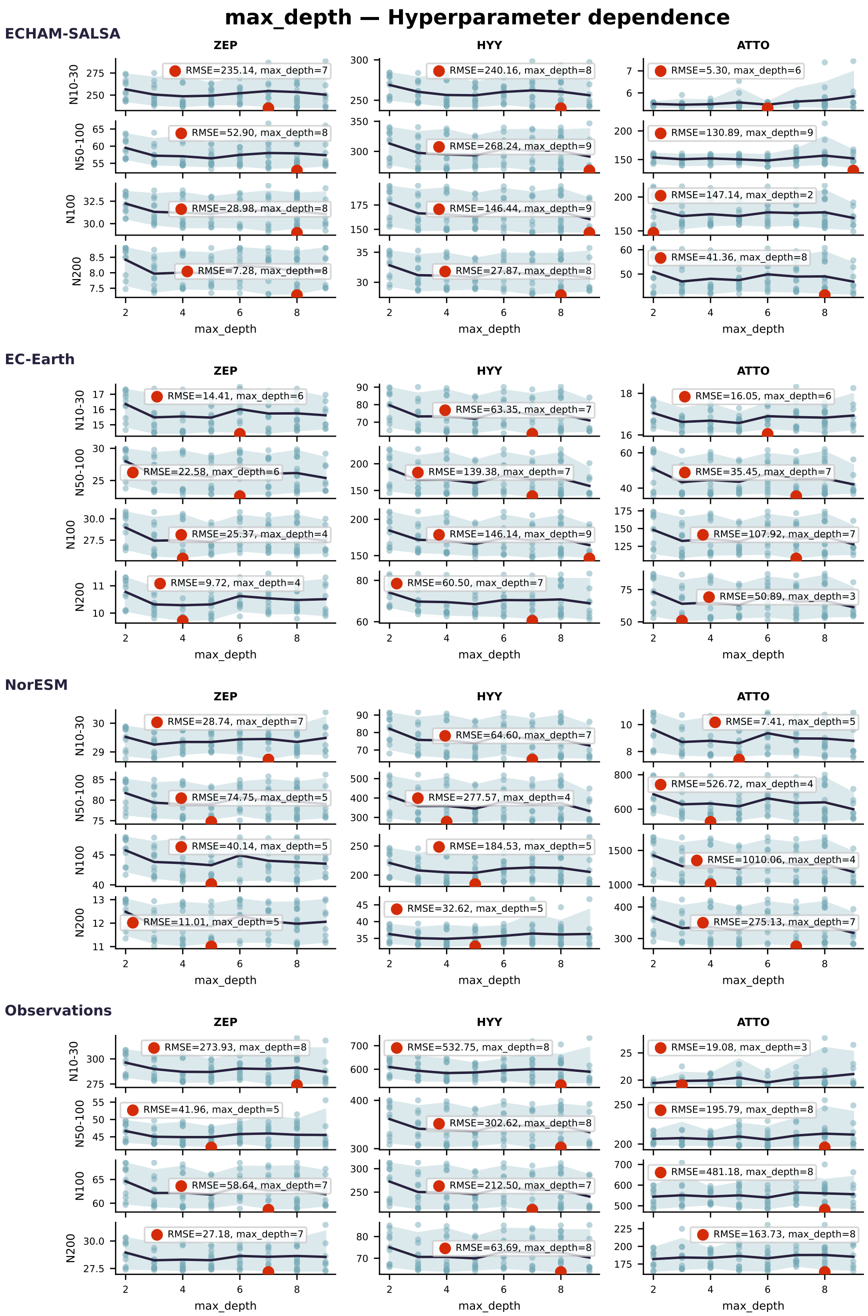

Figure S76. Parameter tuning for XGBoost max_depth.

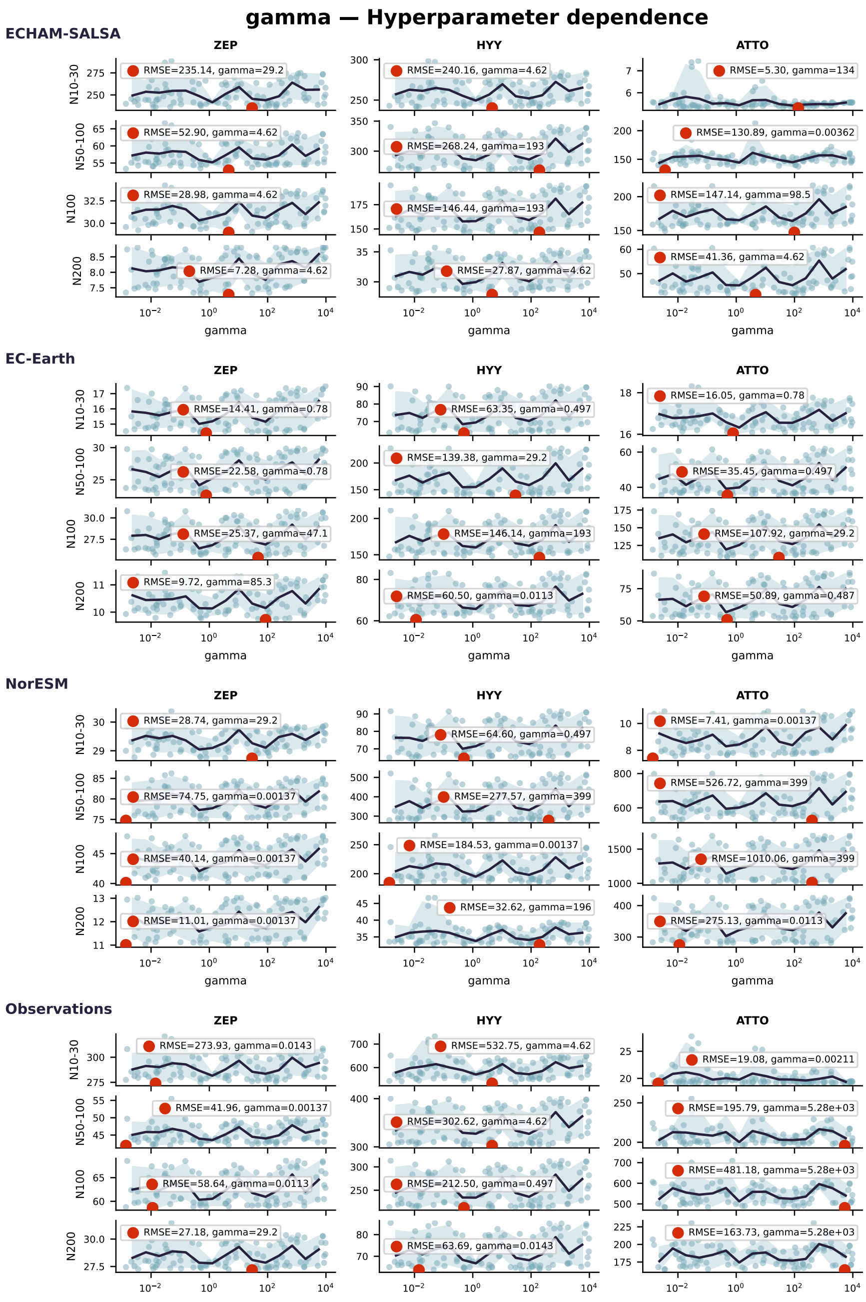

Figure S77. Parameter tuning for XGBoost gamma.

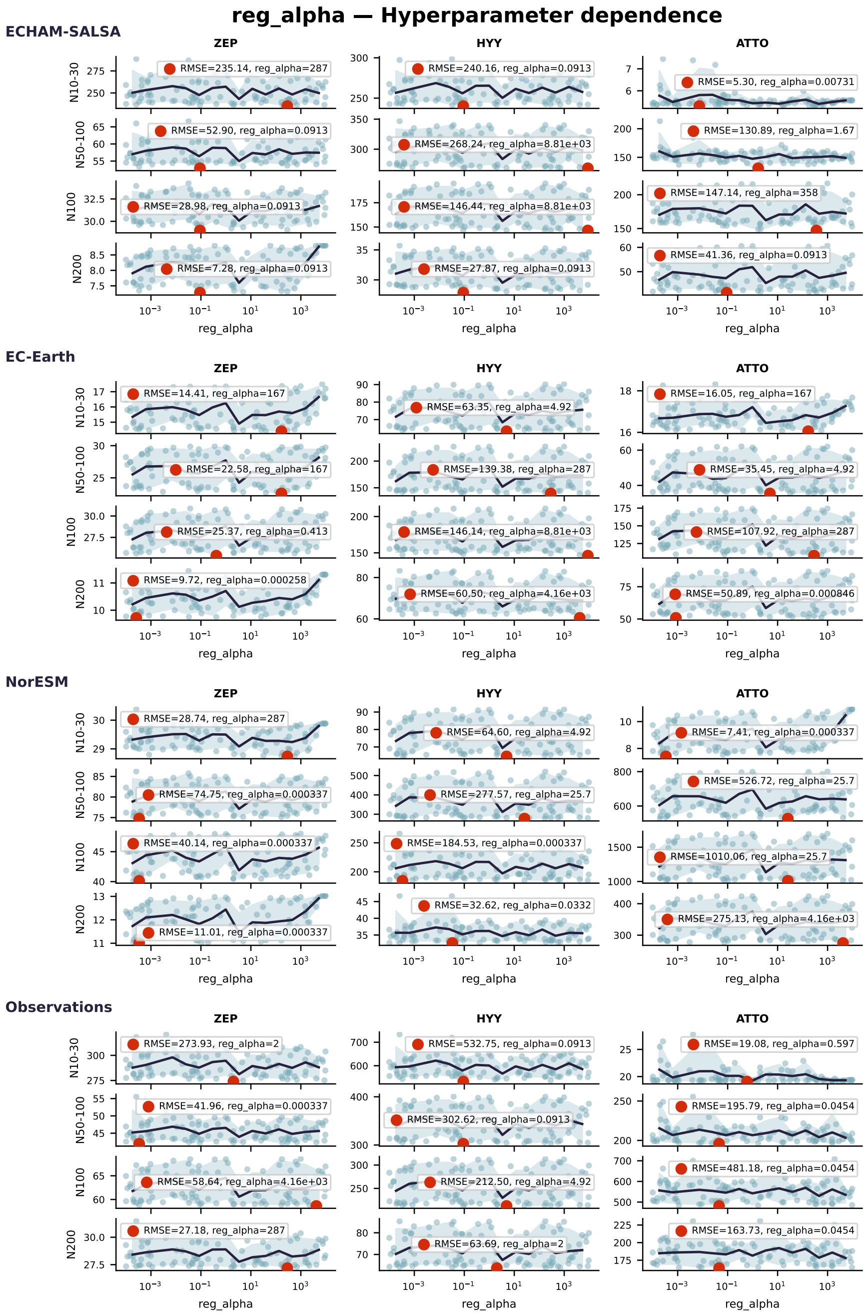

Figure S78. Parameter tuning for XGBoost reg_alpha.

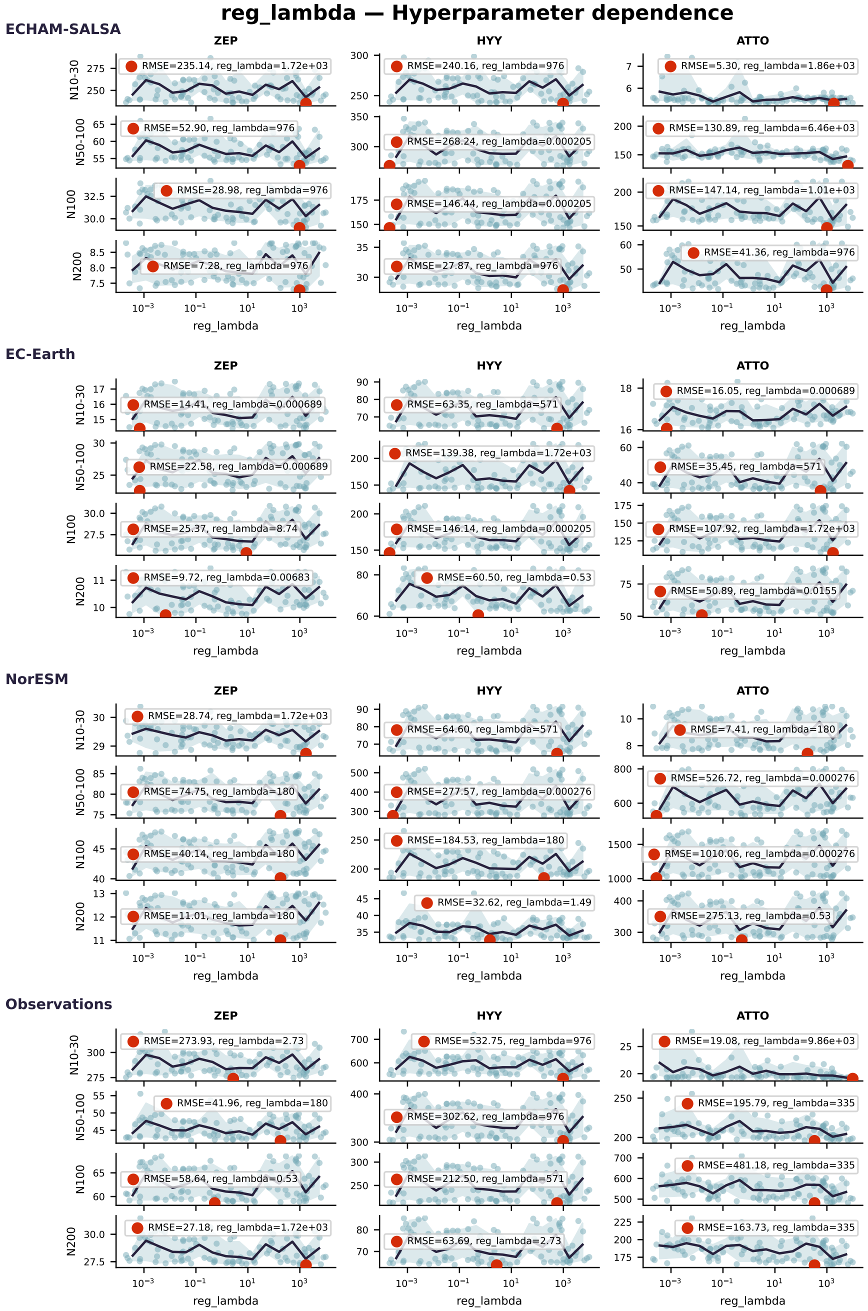

Figure S79. Parameter tuning for XGBoost reg_lambda.

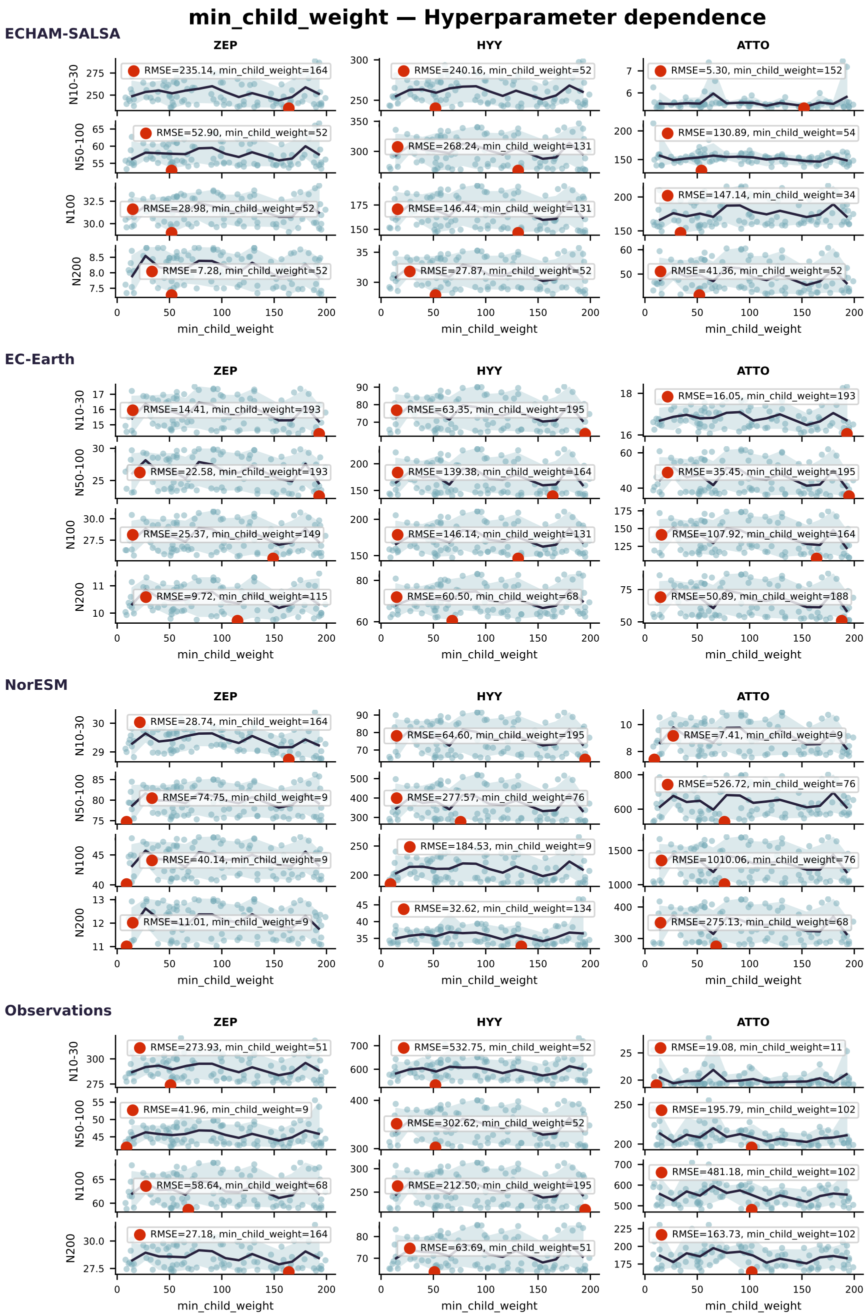

Figure S80. Parameter tuning for XGBoost min_child_weight.

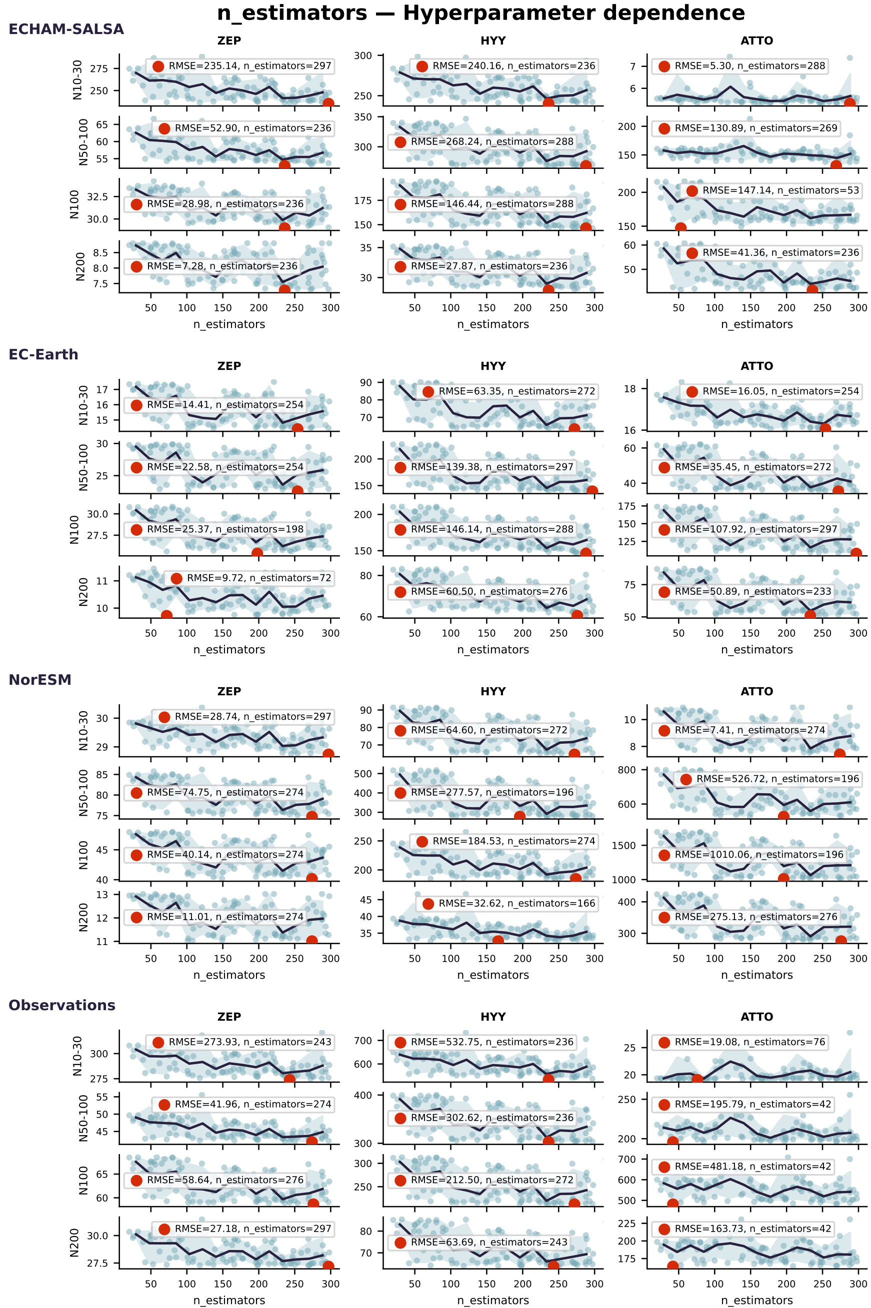

Figure S81. Parameter tuning for XGBoost n_estimators.

Based on the exploration of hyperparameters shown in Figs. S75-S81, the following hyperparameters were chosen for the final XGBoost model: learning_rate=0.1, max_depth=6, gamma=0, reg_alpha=0, reg_lambda=1, min_child_weight=1, n_estimators=300. The hyperparameter that seems to play the strongest role is the learning rate, which for all data sources and models has a minimum around 0.1. For the number of boosting rounds (n_estimators), there is also some improvent with increased number, and we therefore pick 300. For the other parameters, we have selected the default values.

References

Abdul-Razzak, H. and Ghan, S. J.: A Parameterization of Aerosol Activation: 2. Multiple Aerosol Types, Journal of Geophysical Research: Atmospheres, 105, 6837–6844, https://doi.org/10.1029/1999JD901161, 2000.

Abdul-Razzak, H. and Ghan, S. J.: A Parameterization of Aerosol Activation 3. Sectional Representation, Journal of Geophysical Research: Atmospheres, 107, AAC 1–1–AAC 1–6, https://doi.org/10.1029/2001JD000483, 2002.

Balkanski, Y. J., Jacob, D. J., Gardner, G. M., Graustein, W. C., and Turekian, K. K.: Transport and Residence Times of Tropospheric Aerosols Inferred from a Global Three-Dimensional Simulation of 210Pb, Journal of Geophysical Research: Atmospheres, 98, 20 573–20 586, https://doi.org/10.1029/93JD02456, 1993.

Barth, M. C., Rasch, P. J., Kiehl, J. T., Benkovitz, C. M., and Schwartz, S. E.: Sulfur Chemistry in the National Center for Atmospheric Research Community Climate Model: Description, Evaluation, Features, and Sensitivity to Aqueous Chemistry, Journal of Geophysical Research: Atmospheres, 105, 1387–1415, https://doi.org/10.1029/1999JD900773, 2000.

Bentsen, M., Bethke, I., Debernard, J. B., Iversen, T., Kirkevåg, A., Seland, Ø., Drange, H., Roelandt, C., Seierstad, I. A., Hoose, C., and Kristjánsson, J. E.: The Norwegian Earth System Model, NorESM1-M – Part 1: Description and Basic Evaluation of the Physical Climate, Geoscientific Model Development, 6, 687–720, https://doi.org/10.5194/gmd-6-687-2013, 2013.

Bergman, T., Kerminen, V.-M., Korhonen, H., Lehtinen, K. J., Makkonen, R., Arola, A., Mielonen, T., Romakkaniemi, S., Kulmala, M., and Kokkola, H.: Evaluation of the Sectional Aerosol Microphysics Module SALSA Implementation in ECHAM5-HAM Aerosol-Climate Model, Geoscientific Model Development, 5, 845–868, https://doi.org/10.5194/gmd-5-845-2012, 2012.

Berrisford, P., Dee, D. P., Poli, P., Brugge, R., Fielding, M., Fuentes, M., Kållberg, P. W., Kobayashi, S., Uppala, S., and Simmons, A.: The ERA-Interim Archive Version 2.0, 2011.

Bogenschutz, P. A., Gettelman, A., Hannay, C., Larson, V. E., Neale, R. B., Craig, C., and Chen, C.-C.: The Path to CAM6: Coupled Simulations with CAM5.4 and CAM5.5, Geoscientific Model Development, 11, 235–255, https://doi.org/10.5194/gmd-11-235-2018, 2018.

Bourgeois, Q. and Bey, I.: Pollution Transport Efficiency toward the Arctic: Sensitivity to Aerosol Scavenging and Source Regions, Journal of Geophysical Research: Atmospheres, 116, https://doi.org/10.1029/2010JD015096, 2011.

Croft, B., Lohmann, U., Martin, R. V., Stier, P., Wurzler, S., Feichter, J., Posselt, R., and Ferrachat, S.: Aerosol Size-Dependent below-Cloud Scavenging by Rain and Snow in the ECHAM5-HAM, Atmospheric Chemistry and Physics, 9, 4653–4675, https://doi.org/10.5194/acp-9-4653-2009, 2009.

Croft, B., Lohmann, U., Martin, R. V., Stier, P., Wurzler, S., Feichter, J., Hoose, C., Heikkilä, U., van Donkelaar, A., and Ferrachat, S.: Influences of In-Cloud Aerosol Scavenging Parameterizations on Aerosol Concentrations and Wet Deposition in ECHAM5-HAM, Atmospheric Chemistry and Physics, 10, 1511–1543, https://doi.org/10.5194/acp-10-1511-2010, 2010.

Dana, M. T. and Hales, J. M.: Statistical Aspects of the Washout of Polydisperse Aerosols, Atmospheric Environment (1967), 10, 45–50, https://doi.org/10.1016/0004-6981(76)90258-4, 1976.

Danabasoglu, G., Lamarque, J.-F., Bacmeister, J., Bailey, D. A., DuVivier, A. K., Edwards, J., Emmons, L. K., Fasullo, J., Garcia, R., Gettelman, A., Hannay, C., Holland, M. M., Large, W. G., Lauritzen, P. H., Lawrence, D. M., Lenaerts, J. T. M., Lindsay, K., Lipscomb, W. H., Mills, M. J., Neale, R., Oleson, K. W., Otto-Bliesner, B., Phillips, A. S., Sacks, W., Tilmes, S., van Kampenhout, L., Vertenstein, M., Bertini, A., Dennis, J., Deser, C., Fischer, C., Fox-Kemper, B., Kay, J. E., Kinnison, D., Kushner, P. J., Larson, V. E., Long, M. C., Mickelson, S., Moore, J. K., Nienhouse, E., Polvani, L., Rasch, P. J., and Strand, W. G.: The Community Earth System Model Version 2 (CESM2), Journal of Advances in Modeling Earth Systems, 12, e2019MS001 916, https://doi.org/10.1029/2019MS001916, 2020.

de Bruine, M., Krol, M., van Noije, T., Le Sager, P., and Röckmann, T.: The Impact of Precipitation Evaporation on the Atmospheric Aerosol Distribution in EC-Earth v3.2.0, Geoscientific Model Development, 11, 1443–1465, https://doi.org/10.5194/gmd-11-1443-2018, 2018.

Döscher, R., Acosta, M., Alessandri, A., Anthoni, P., Arsouze, T., Bergman, T., Bernardello, R., Boussetta, S., Caron, L.-P., Carver, G., Castrillo, M., Catalano, F., Cvijanovic, I., Davini, P., Dekker, E., Doblas-Reyes, F. J., Docquier, D., Echevarria, P., Fladrich, U., Fuentes-Franco, R., Gröger, M., v. Hardenberg, J., Hieronymus, J., Karami, M. P., Keskinen, J.-P., Koenigk, T., Makkonen, R., Massonnet, F., Ménégoz, M., Miller, P. A., Moreno-Chamarro, E., Nieradzik, L., van Noije, T., Nolan, P., O'Donnell, D., Ollinaho, P., van den Oord, G., Ortega, P., Prims, O. T., Ramos, A., Reerink, T., Rousset, C., Ruprich-Robert, Y., Le Sager, P., Schmith, T., Schrödner, R., Serva, F., Sicardi, V., Sloth Madsen, M., Smith, B., Tian, T., Tourigny, E., Uotila, P., Vancoppenolle, M., Wang, S., Wårlind, D., Willén, U., Wyser, K., Yang, S., Yepes-Arbós, X., and Zhang, Q.: The EC-Earth3 Earth System Model for the Coupled Model Intercomparison Project 6, Geoscientific Model Development, 15, 2973–3020, https://doi.org/10.5194/gmd-15-2973-2022, 2022.

Gettelman, A. and Morrison, H.: Advanced Two-Moment Bulk Microphysics for Global Models. Part I: Off-Line Tests and Comparison with Other Schemes, Journal of Climate, 28, 1268–1287, https://doi.org/10.1175/JCLI-D-14-00102.1, 2015.

Holopainen, E., Kokkola, H., Laakso, A., and Kühn, T.: In-Cloud Scavenging Scheme for Sectional Aerosol Modules – Implementation in the Framework of the Sectional Aerosol Module for Large Scale Applications Version 2.0 (SALSA2.0) Global Aerosol Module, Geoscientific Model Development, 13, 6215–6235, https://doi.org/10.5194/gmd-13-6215-2020, 2020.

Hurrell, J. W., Hack, J. J., Shea, D., Caron, J. M., and Rosinski, J.: A New Sea Surface Temperature and Sea Ice Boundary Dataset for the Community Atmosphere Model, Journal of Climate, 21, 5145–5153, https://doi.org/10.1175/2008JCLI2292.1, 2008.

Irfan, M., Kühn, T., Yli-Juuti, T., Laakso, A., Holopainen, E., Worsnop, D. R., Virtanen, A., and Kokkola, H.: A Model Study Investigating the Sensitivity of Aerosol Forcing to the Volatilities of Semi-Volatile Organic Compounds, Atmospheric Chemistry and Physics, 24, 8489–8506, https://doi.org/10.5194/acp-24-8489-2024, 2024.

Iversen, T., Bentsen, M., Bethke, I., Debernard, J. B., Kirkevåg, A., Seland, Ø., Drange, H., Kristjansson, J. E., Medhaug, I., Sand, M., and Seierstad, I. A.: The Norwegian Earth System Model, NorESM1-M – Part 2: Climate Response and Scenario Projections, Geoscientific Model Development, 6, 389–415, https://doi.org/10.5194/gmd-6-389-2013, 2013.

Kirkevåg, A., Iversen, T., Seland, Ø., Hoose, C., Kristjánsson, J. E., Struthers, H., Ekman, A. M. L., Ghan, S., Griesfeller, J., Nilsson, E. D., and Schulz, M.: Aerosol–Climate Interactions in the Norwegian Earth System Model – NorESM1-M, Geosci. Model Dev., 6, 207–244, https://doi.org/10.5194/gmd-6-207-2013, 2013.

Kirkevåg, A., Grini, A., Olivié, D., Seland, Ø., Alterskjær, K., Hummel, M., Karset, I. H. H., Lewinschal, A., Liu, X., Makkonen, R., Bethke, I., Griesfeller, J., Schulz, M., and Iversen, T.: A Production-Tagged Aerosol Module for Earth System Models, OsloAero5.3 – Extensions and Updates for CAM5.3-Oslo, Geoscientific Model Development, 11, 3945–3982, https://doi.org/10.5194/gmd-11-3945-2018, 2018.

Kokkola, H., Kühn, T., Laakso, A., Bergman, T., Lehtinen, K. E. J., Mielonen, T., Arola, A., Stadtler, S., Korhonen, H., Ferrachat, S., Lohmann, U., Neubauer, D., Tegen, I., Siegenthaler-Le Drian, C., Schultz, M. G., Bey, I., Stier, P., Daskalakis, N., Heald, C. L., and Romakkaniemi, S.: SALSA2.0: The Sectional Aerosol Module of the Aerosol–Chemistry–Climate Model ECHAM6.3.0-HAM2.3-MOZ1.0, Geoscientific Model Development, 11, 3833–3863, https://doi.org/10.5194/gmd-11-3833-2018, 2018.

Krol, M., Houweling, S., Bregman, B., van den Broek, M., Segers, A., van Velthoven, P., Peters, W., Dentener, F., and Bergamaschi, P.: The Two-Way Nested Global Chemistry-Transport Zoom Model TM5: Algorithm and Applications, Atmospheric Chemistry and Physics, 5, 417–432, https://doi.org/10.5194/acp-5-417-2005, 2005.

Machado, L. A. T., Unfer, G. R., Brill, S., Hildmann, S., Pöhlker, C., Cheng, Y., Williams, J., Hartwig, H., Andreae, M. O., Artaxo, P., Curtius, J., Franco, M. A., Cecchini, M. A., Edtbauer, A., Hoffmann, T., Holanda, B., Khadir, T., Krejci, R., Kremper, L. A., Liu, Y., Meller, B. B., Pöhlker, M. L., Quesada, C. A., Ringsdorf, A., Riipinen, I., Trumbore, S., Wolff, S., Lelieveld, J., and Pöschl, U.: Frequent Rainfall-Induced New Particle Formation within the Canopy in the Amazon Rainforest, Nature Geoscience, 17, 1225–1232, https://doi.org/10.1038/s41561-024-01585-0, 2024.

Marshall, J. S. and Palmer, W. M. K.: THE DISTRIBUTION OF RAINDROPS WITH SIZE, 1948.

Mielonen, T., Hienola, A., Kühn, T., Merikanto, J., Lipponen, A., Bergman, T., Korhonen, H., Kolmonen, P., Sogacheva, L., Ghent, D., Pitkänen, M. R. A., Arola, A., De Leeuw, G., and Kokkola, H.: Summertime Aerosol Radiative Effects and Their Dependence on Temperature over the Southeastern USA, Atmosphere, 9, 180, https://doi.org/10.3390/atmos9050180, 2018.

Rayner, N. A., Parker, D. E., Horton, E. B., Folland, C. K., Alexander, L. V., Rowell, D. P., Kent, E. C., and Kaplan, A.: Global Analyses of Sea Surface Temperature, Sea Ice, and Night Marine Air Temperature since the Late Nineteenth Century, Journal of Geophysical Research: Atmospheres, 108, https://doi.org/10.1029/2002JD002670, 2003.

Schultz, M. G., Stadtler, S., Schröder, S., Taraborrelli, D., Franco, B., Krefting, J., Henrot, A., Ferrachat, S., Lohmann, U., Neubauer, D., Siegenthaler-Le Drian, C., Wahl, S., Kokkola, H., Kühn, T., Rast, S., Schmidt, H., Stier, P., Kinnison, D., Tyndall, G. S., Orlando, J. J., and Wespes, C.: The Chemistry–Climate Model ECHAM6.3-HAM2.3-MOZ1.0, Geosci. Model Dev., 11, 1695–1723, https://doi.org/10.5194/gmd-11-1695-2018, 2018.

Seland, Ø., Bentsen, M., Olivié, D., Toniazzo, T., Gjermundsen, A., Graff, L. S., Debernard, J. B., Gupta, A. K., He, Y.-C., Kirkevåg, A., Schwinger, J., Tjiputra, J., Aas, K. S., Bethke, I., Fan, Y., Griesfeller, J., Grini, A., Guo, C., Ilicak, M., Karset, I. H. H., Landgren, O., Liakka, J., Moseid, K. O., Nummelin, A., Spensberger, C., Tang, H., Zhang, Z., Heinze, C., Iversen, T., and Schulz, M.: Overview of the Norwegian Earth System Model (NorESM2) and Key Climate Response of CMIP6 DECK, Historical, and Scenario Simulations, Geoscientific Model Development, 13, 6165–6200, https://doi.org/10.5194/gmd-13-6165-2020, 2020.

Stier, P., Feichter, J., Kinne, S., Kloster, S., Vignati, E., Wilson, J., Ganzeveld, L., Tegen, I., Werner, M., Balkanski, Y., Schulz, M., Boucher, O., Minikin, A., and Petzold, A.: The Aerosol-Climate Model ECHAM5-HAM, Atmospheric Chemistry and Physics, 5, 1125–1156, https://doi.org/10.5194/acp-5-1125-2005, 2005.

Tegen, I., Neubauer, D., Ferrachat, S., Siegenthaler-Le Drian, C., Bey, I., Schutgens, N., Stier, P., Watson-Parris, D., Stanelle, T., Schmidt, H., Rast, S., Kokkola, H., Schultz, M., Schroeder, S., Daskalakis, N., Barthel, S., Heinold, B., and Lohmann, U.: The Global Aerosol–Climate Model ECHAM6.3–HAM2.3 – Part 1: Aerosol Evaluation, Geoscientific Model Development, 12, 1643–1677, https://doi.org/10.5194/gmd-12-1643-2019, 2019.

van Noije, T., Bergman, T., Le Sager, P., O'Donnell, D., Makkonen, R., Gonçalves-Ageitos, M., Döscher, R., Fladrich, U., von Hardenberg, J., Keskinen, J.-P., Korhonen, H., Laakso, A., Myriokefalitakis, S., Ollinaho, P., Pérez García-Pando, C., Reerink, T., Schrödner, R., Wyser, K., and Yang, S.: EC-Earth3-AerChem: A Global Climate Model with Interactive Aerosols and Atmospheric Chemistry Participating in CMIP6, Geoscientific Model Development, 14, 5637–5668, https://doi.org/10.5194/gmd-14-5637-2021, 2021.

van Noije, T. P. C., Le Sager, P., Segers, A. J., van Velthoven, P. F. J., Krol, M. C., Hazeleger, W., Williams, A. G., and Chambers, S. D.: Simulation of Tropospheric Chemistry and Aerosols with the Climate Model EC-Earth, Geoscientific Model Development, 7, 2435–2475, https://doi.org/10.5194/gmd-7-2435-2014, 2014.

Vignati, E., Wilson, J., and Stier, P.: M7: An Efficient Size-Resolved Aerosol Microphysics Module for Large-Scale Aerosol Transport Models: AEROSOL MICROPHYSICS MODULE, Journal of Geophysical Research: Atmospheres, 109, n/a–n/a, https://doi.org/10.1029/2003JD004485, 2004.

Williams, J. E., Boersma, K. F., Le Sager, P., and Verstraeten, W. W.: The High-Resolution Version of TM5-MP for Optimized Satellite Retrievals: Description and Validation, Geoscientific Model Development, 10, 721–750, https://doi.org/10.5194/gmd-10-721-2017, 2017.

Zhang, G. J. and McFarlane, N. A.: Sensitivity of Climate Simulations to the Parameterization of Cumulus Convection in the Canadian Climate Centre General Circulation Model, Atmosphere-Ocean, 33, 407–446, https://doi.org/10.1080/07055900.1995.9649539, 1995.

Zhang, K., O'Donnell, D., Kazil, J., Stier, P., Kinne, S., Lohmann, U., Ferrachat, S., Croft, B., Quaas, J., Wan, H., Rast, S., and Feichter, J.: The Global Aerosol-Climate Model ECHAM-HAM, Version 2: Sensitivity to Improvements in Process Representations, Atmospheric Chemistry and Physics, 12, 8911–8949, https://doi.org/10.5194/acp-12-8911-2012, 2012.